
PRACTICAL MULTI-FIDELITY MACHINE LEARNING: FUSION OF DETERMINISTIC AND BAYESIAN MODELS

Jiaxiang Yi

Faculty of Mechanical Engineering
Delft University of Technology
Mekelweg 2, Delft, 2628 CD, The Netherlands
J.Yi@tudelft.nl

Ji Cheng

Department of Computer Science
City University of Hong Kong
83 Tat Chee Avenue, Kowloon, Hong Kong
jicheng9617@gmail.com

Miguel A. Bessa

School of Engineering
Brown University
184 Hope St., Providence, RI 02912, USA
miguel_bessa@brown.edu

July 23, 2024

ABSTRACT

Multi-fidelity machine learning methods address the accuracy-efficiency trade-off by integrating scarce, resource-intensive high-fidelity data with abundant but less accurate low-fidelity data. We propose a practical multi-fidelity strategy for problems spanning low- and high-dimensional domains, integrating a non-probabilistic regression model for the low-fidelity with a Bayesian model for the high-fidelity. The models are trained in a staggered scheme, where the low-fidelity model is transfer-learned to the high-fidelity data and a Bayesian model is trained for the residual. This three-model strategy – deterministic low-fidelity, transfer learning, and Bayesian residual – leads to a prediction that includes uncertainty quantification both for noisy and noiseless multi-fidelity data. The strategy is general and unifies the topic, highlighting the expressivity trade-off between the transfer-learning and Bayesian models (a complex transfer-learning model leads to a simpler Bayesian model, and vice versa). We propose modeling choices for two scenarios, and argue in favor of using a linear transfer-learning model that fuses 1) kernel ridge regression for low-fidelity with Gaussian processes for high-fidelity; or 2) deep neural network for low-fidelity with a Bayesian neural network for high-fidelity. We demonstrate the effectiveness and efficiency of the proposed strategies and contrast them with the state-of-the-art based on various numerical examples. The simplicity of these formulations makes them practical for a broad scope of future engineering applications.

Keywords Bayesian machine learning · Multi-fidelity modeling · Uncertainty quantification · Gaussian process regression

1 Introduction

Expressive non-probabilistic machine learning methods, such as deep neural networks (DNNs), are able to approximate any nonlinear continuous function, provided enough data [1]. However, they can be prone to over-fitting, especially in the presence of noisy data [2], and are not able to predict uncertainty. Bayesian Machine Learning (BML) methods do not have these limitations [3], although their training requires additional computational effort. In this article, we present a practical multi-fidelity (MF) strategy that combines non-probabilistic low-fidelity (LF) surrogates and Bayesian residual surrogates. We demonstrate the simplicity of the proposed MF strategy and consider two common regression scenarios encountered in engineering practice: (1) low-dimensional problems amenable to models with few hyperparameters and easy training; and (2) high-dimensional problems that require more expressive models and involve additional training effort.

MF data arises naturally in most engineering applications. High-fidelity (HF) data is often associated with costly and time-consuming experiments, or with accurate yet computationally expensive simulations. In contrast, LF data is usually obtained by efficient strategies (experimental [4], analytical [5], or computational [6, 7]) at the expense of accuracy. Therefore, LF data is typically acquired faster, often by several orders of magnitude. Using both datasets can be advantageous to train better models as long as the loss in fidelity is compensated by the presence of more low-fidelity data.

The challenges associated with developing MF regression models arise from the need to define one regression model (a surrogate) per fidelity, and in the subsequent definition of the interaction between these models [8, 9]. Without loss of generality, we focus on MF regression models with only two levels of fidelity. We start by introducing MF regression in a general form and by quickly reviewing common choices for surrogate models. We continue by reviewing common MF strategies, which involve the same type of surrogate model across fidelities. Then, we propose two MF strategies using non-probabilistic LF regression models together with Bayesian residual models.

Summary of contributions. We introduce a general framework for MF regression and demonstrate its versatility. We hypothesize that most MF regression cases in practice can be covered by considering simple linear regression (LR) transfer-learning models and the following two options for low- and high-fidelity models: 1) kernel ridge regression (KRR) and Gaussian process regression (GPR), leading to the KRR-LR-GPR model; or 2) a deep neural network (DNN) and a Bayesian neural network (BNN), leading to the DNN-LR-BNN model. The KRR-LR-GPR model has few parameters and hyperparameters, facilitating training but limiting scalability (limits on data dimension and size, as well as training and inference time). The DNN-LR-BNN model is more flexible and more challenging to train, but it is applicable for low- and high-dimensional data with few scalability limits. The simpler model (KRR-LR-GPR) should be used when possible, while the DNN-LR-BNN model is expected to be applicable to most practical cases. In the limit of having complex correlations between low- and high-fidelity, a DNN-BNN model can be used where the BNN takes care of both transfer-learning and residual modeling, although this leads to the most difficult model to train and is expected to have narrower applicability.

2 Methodology and related work

For simplicity of notation, we start by considering datasets with d -dimensional inputs \mathbf{x} but one-dimensional output y . Then, the LF dataset contains \mathbf{x}_n^l input and y_n^l output points, where $n = 1, \dots, N^l$ are the N^l points in this dataset (the superscript l refers to low-fidelity). The HF dataset is equivalently defined by \mathbf{x}_n^h and y_n^h , where $n = 1, \dots, N^h$ are the N^h HF points in this dataset. In this article, we define a MF regression model $f^h(\mathbf{x})$ as a conjunction of three models: (1) the LF model $f^l(\mathbf{x})$ that is trained on LF data $\{\mathbf{x}^l, y^l\}$; (2) a transfer-learning model $g(\mathbf{x})$ that transforms the LF model to the HF data; (3) a residual model $r(\mathbf{x})$ (if necessary) that captures the difference between transfer-learned LF model and the HF data. Therefore, a general description can be formulated as:

$$f^h(\mathbf{x}) = g(f^l(\mathbf{x}), \mathbf{x}) + r(\mathbf{x}) \quad (1)$$

In the data-scarce literature [10, 11], MF models use GPRs for both $f^l(\mathbf{x})$ and $r(\mathbf{x})$ and consider a linear transfer-learning model $g(\mathbf{x}) := g(f^l(\mathbf{x})) = f^l(\mathbf{x})\rho$, such that:

$$f^h(\mathbf{x}) = f^l(\mathbf{x})\rho + r(\mathbf{x}) \quad (2)$$

where ρ is a single hyperparameter that transforms the LF model $f^l(\mathbf{x})$ to the HF responses.

Other investigations focus on using a transfer-learning LF model of higher complexity, for example, Bayesian models [12, 13], while setting $r(\mathbf{x}) := 0$, leading to:

$$f^h(\mathbf{x}) = g(f^l(\mathbf{x}), \mathbf{x}) \quad (3)$$

Here, we argue in favor of generalizing these modeling assumptions by establishing a simple transfer-learning model $g(\mathbf{x})$ that is trained on HF data, and by choosing an appropriate deterministic low-fidelity model $f^l(\mathbf{x})$ and a Bayesian high-fidelity residual $r(\mathbf{x})$.

2.1 Related work for data-scarce scenarios

In the data-scarce regime, GPR or Kriging [14] stand out due to their elegant derivation and exact integration for Gaussian likelihoods and priors (see Appendix A.2 for a short introduction). Early in their development, GPR was extended to handle MF problems according to Eq. (2), in a method originally called Co-Kriging [15, 16]. This method is based on expanding the covariance function of GPRs in the form of

$$\mathbf{C} = \begin{bmatrix} \mathbf{K}(\mathbf{X}^h, \mathbf{X}^h) & \mathbf{K}(\mathbf{X}^h, \mathbf{X}^l) \\ \mathbf{K}(\mathbf{X}^l, \mathbf{X}^h) & \mathbf{K}(\mathbf{X}^l, \mathbf{X}^l) \end{bmatrix}$$

Different variants of this formulation can be found, including multi-task GPR [11, 17] that consider more than one output, or latent mapping GPR for cases with categorical variables [18, 19]. Unfortunately, Co-Kriging has complexity of order $\mathcal{O}((N^l + N^h)^3)$ due to the inversion involved when calculating the determinants of the covariance matrix \mathbf{C} , imposing practical limits on the number of data points and the dimensionality [20, 10, 21, 22]. To this end, Hierarchical Kriging [23] and corresponding variants [24, 25, 17] considering a diagonal sub-matrix of \mathbf{C} have been proposed. For example, Scale Kriging [26, 27] assumes a fixed hyperparameter for the transfer model, i.e. $\rho = 1$, while recursive Co-Kriging [28] uses fast cross-validation for identifying parameters. In practice, however, it can be challenging to strike a balance between applying MF-GPR to large datasets (improving complexity) without degrading performance significantly [29, 30]. Furthermore, the literature is scarce on their application to noisy MF data [31].

We also note that there are other methods of interest in data-scarce MF problems. For example, a MF polynomial chaos expansion model [31] that also relies on Eq. (2) has recently been proposed. The method was demonstrated for noisy HF data, but considering noiseless LF data. The scalability of these approaches is mainly limited by the amount of LF data, usually several times more than that of HF data. In contrast, deterministic MF models have shown better scalability at the sacrifice of not predicting uncertainty. Examples include MF linear regression [32], MF Radial Basis Kernel (RBF) regression [33], and MF support vector regression [34]. Yet, the combination of deterministic and Bayesian models for MF regression merits further investigation.

2.2 Related work for data-rich scenarios

Machine learning models trained on data-rich MF datasets can be seen in different contexts, for instance, assisting design [35, 36], optimization [37], and in uncertainty quantification [38]. Focusing on regression problems, deterministic models such as DNNs have been shown to obtain a reasonable point estimate instead of the full posterior. For example, the MF-DNN approach proposed by Aydin et al. [39] sequentially passes data from the LF to the HF into the same DNN with an error metric for fidelity switching. Transfer learning based on MF dataset [40, 41] uses the LF dataset to pre-train the weights of a DNN and then shifts to the HF dataset to finalize training. Other examples include a MF Graph Neural Network (GNN) developed by Black et al. [42], and a MF-DNN architecture introduced by Motamed et al. [38] that establishes the correlation between the HF and LF models via a neural network. Other strategies have involved the concatenation of LF- and HF-DNNs [43, 44, 12], as well as Recurrent Neural Networks [45], and Convolutional Neural Networks [46].

Although deterministic MF-DNNs are common in the literature, they are ineffective in predicting uncertainty, are prone to over-fitting, and do not provide a principled way to handle noisy data [13, 44, 43]. Instead, BNNs [47] provide a theoretical framework that naturally addresses these limitations but introduces a few other issues. In particular, the integration of the posterior distribution and the posterior predictive distribution (PPD) is intractable analytically. Usually, Bayesian inference approaches such as Markov Chain Monte Carlo (MCMC) [47, 48], Variational Inference (VI) [49], Monte Carlo Dropout [50], among many others [51] are used for integrating the posterior distribution. However, the prohibitive training and inference time limits the adoption of MF-BNNs as opposed to MF-DNNs. Recent work has shown promise, for example, Meng et al. [13] extended their previous concatenated MF-DNN architecture [43] by replacing the HF DNN with a BNN and using Hamiltonian Monte Carlo to perform inference in a reasonable amount of time [52, 53]. Still, its effectiveness has only been demonstrated in low-dimensional examples. In addition, Baptiste et al. [54] proposed to use both Bayesian models for HF and LF datasets, where a GPR was used in the LF and a BNN was used in HF. However, they cautioned that the strategy was only suitable for solving low-dimensional problems because

of the time-consuming inference procedure. In summary, considering BNNs in the context of MF data is challenging due to the trade-off between inference time and accuracy. Although in theory, using both BNNs for LF and HF datasets is possible, it has also been shown that the inference time can be worse than a simple combination of a GPR and a BNN [54]. Furthermore, despite considering different architectures, most rely on the linear model of Eq. (2), and they are applied in the data-scarce scenario without considering noisy data, especially at the LF level.

3 Practical multi-fidelity Bayesian machine learning (MF-BML)

In practice, creating a MF model involves so many choices [10, 11] that it is difficult to perform principled model selection and hyperparameter optimization, especially for large datasets. We propose a simple strategy summarized in Eq. (2) to develop practical MF models based on two ideas, as shown in Fig. 1. First, consider a deterministic LF model $f^l(\mathbf{x})$ together with a probabilistic model of the residual $r(\mathbf{x})$. Second, consider a transfer-learning model $g(\mathbf{x})$ as a simple linear regression whose basis function is the LF model. As we demonstrate in the remainder of the paper, the proposed strategy leverages the advantages of deterministic and probabilistic models while keeping the transfer learning model simple.

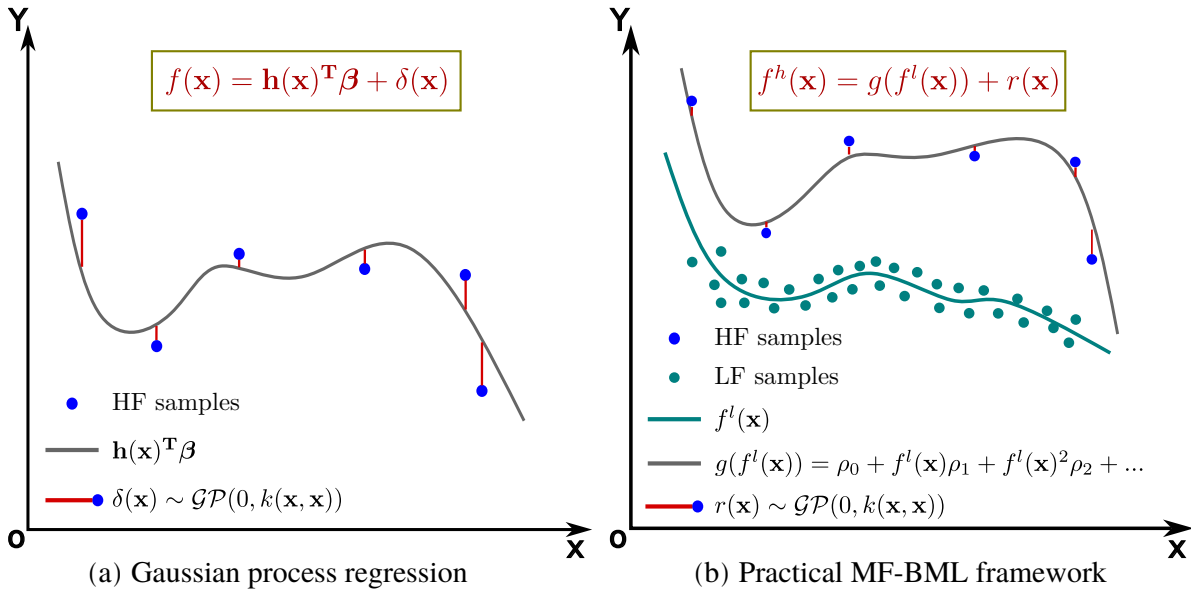


Figure 1: Illustration of how the practical MF-BML evolves from GPR. (a) GPR with explicit basis function, in which a first linear regression is executed based on the basis function $\mathbf{h}(\mathbf{x}) = [1, \mathbf{x}, \mathbf{x}^2, \dots]^T$ and where $\delta(\mathbf{x})$ is assumed to be a zero mean GPR for characterizing the residual. (b) the practical MF-BML follows the same concept by utilizing the LF surrogate as the basis. A linear transfer-learning function on $f^l(\mathbf{x})$ adjusts the prediction for the HF, and facilitates the determination of the residual $r(\mathbf{x})$ by a Bayesian model with a simple prior.

Thus, the transfer-learning model $g(\mathbf{x})$ in Eq. (2) is proposed to be linear (in the weights) but considering its basis functions as the LF model. In the case of considering only one LF model, we write the proposed MF-BML model as follows:

$$f^h(\mathbf{x}) = g(f^l(\mathbf{x})) + r(\mathbf{x}) \quad (4)$$

$$= \mathbf{m}(\mathbf{x})^T \boldsymbol{\rho} + r(\mathbf{x}) \quad (5)$$

$$= \rho_0 + f^l(\mathbf{x})\rho_1 + f^l(\mathbf{x})^2\rho_2 + \dots + f^l(\mathbf{x})^{M-1}\rho_{M-1} + r(\mathbf{x}) \quad (6)$$

where $\mathbf{m}(\mathbf{x}) = [1, f^l(\mathbf{x}), f^l(\mathbf{x})^2, \dots, f^l(\mathbf{x})^{M-1}]^T$ is the vector with M polynomial basis formed with the LF model, and $\boldsymbol{\rho} = [\rho_0, \rho_1, \dots, \rho_{M-1}]^T$ is the corresponding coefficient vector to be determined from training on the HF data, i.e. these coefficients are not imposed as hyperparameters. As previously mentioned in Section 2.1, a majority of MF models simplify the transfer-learning model to become linear, i.e. they reduce Eq. (4) to Eq. (2) by considering $\mathbf{m}(\mathbf{x}) = f^l(\mathbf{x})$ and then considering ρ_1 as a hyperparameter.

In addition to defining the transfer-learning model, there are many possible choices for LF and HF models. Table 1 summarizes common models, as reviewed in the introduction. We suggest two different MF model choices for spanning

a large number of data-scarce and data-rich MF regression problems: 1) kernel ridge regression together with Gaussian process regression (KRR-LR-GPR)¹ for data-scarce or low-dimensionality scenarios; and 2) deep neural network together with a Bayesian neural network (DNN-LR-BNN) for data-rich scenarios.

Table 1: Candidates for LF and HF surrogates within the MF-BML framework

LF surrogates	HF surrogates
Linear regression (LR)	Gaussian process regression (GPR)
Kernel ridge regression (KRR)	Polynomial chaos expansion (PCE)
Deep neural network (DNN)	Bayesian neural network (BNN)
Support Vector Regression (SVR)	...
Gaussian process regression (GPR)*	
Polynomial chaos expansion (PCE)*	
...	

* Often used in conjunction with the same model at the HF, and considering $\mathbf{m}(\mathbf{x}) = f^l(\mathbf{x})$. Examples: GPR-LR-GPR in the form of Co-Kriging [15] or Hierarchical Kriging [23]; PCE-LR-PCE [31]; among others [27].

Remark 1 *There is an advantage in choosing a deterministic LF model because it only acts as a trend function that is transformed by a transfer-learning function, leading to $f^h(\mathbf{x}) - r(\mathbf{x})$. Such LF models can be efficiently trained due to their lower complexity (better scalability) when compared to probabilistic models, handling large LF datasets with or without noise, but without characterizing uncertainty.*

Remark 2 *Choosing a probabilistic model that complements the deterministic LF model, it is possible to make HF prediction that include uncertainty quantification while harnessing the typical advantages of probabilistic models: less prone to overfitting and better approximation quality even in the presence of few HF data.*

3.1 Model for data-scarce or low-dimensional scenarios: KRR-LR-GPR

GPRs are one of the most successful models for data-scarce scenarios [14], having only a few hyperparameters and performing Bayesian inference for Gaussian observation distributions and priors without needing numerical integration. Consequently, they are easy to train for small datasets, making them an important HF model.

We argue that a logical LF model to pair with GPRs in a data-scarce MF scenario is kernel ridge regression (KRR), i.e. the deterministic formulation of GPR [16]. KRR is a kernel machine learning method that is a point estimate of a GPR with the same kernel, therefore also equivalent to a DNN with an infinitely wide hidden layer [55]. KRR is robust to noisy data, and easy to train due to having few hyperparameters. More importantly, existing KRR approaches can lower the time complexity to a range between $\mathcal{O}(n^2)$ and $\mathcal{O}(n)$ by combining proper matrix decomposition technique for matrix inversion, thus handling larger datasets than Polynomial chaos expansion (PCE) or GPR [56, 57] – invaluable for LF datasets because they are typically larger than HF ones. Other LF models such as linear regression or deep neural networks (e.g., see Table 1) have important drawbacks. Linear regression models are sensitive to the choice of the basis functions (often considered to be polynomials whose order is a hyperparameter); this is why we argue for their use as a simple transfer-learning model $g(\mathbf{x})$ but not as a LF or residual model. Conversely, DNNs have a large number of hyperparameters and are therefore less practical to train. Good practice involves starting with simpler models such as KRR that are easier to train and only considering DNNs when the simpler methods fail. We note that GPRs can also be a good choice for a LF model if the LF dataset is small (typically below a few thousand points for most common hardware), but training and inference time increases when compared to KRR, as demonstrated later in this article.

A common kernel of choice for both KRR and GPR when there is not enough prior information is the RBF kernel [16]:

$$k(\mathbf{x}^i, \mathbf{x}^j) = \exp \left(- \sum_{c=1}^d \theta_c (x_c^i - x_c^j)^2 \right) \quad (7)$$

where θ is a d -dimensional vector that controls the length scale of each dimension.

¹Naming convention for the MF model (<LF>-<transfer-learning>-<residual>): the abbreviation on the left is the surrogate for the LF model, the middle is the transfer-learning model, the last abbreviation is the model for the residual. In the absence of one of the models, for example not considering the residual, then the abbreviation only has two models (e.g. DNN-BNN refers to a deep neural network model for LF with a BNN doing the transfer-learning and no residual).

The proposed KRR-LR-GPR established on Eq. (6) is easy to implement and the main steps are listed in Algorithm 1, while additional details are provided in Appendix B. Recall that the key idea is to train a GPR model where, instead of considering a zero mean function, we assume it to be a linear model whose features are the LF model. This is advantageous as there is an explicit solution for finding the parameters ρ from the HF data, no longer treating them as hyperparameters: Step 2.1 in Algorithm 1 or Eq. (24) in the Appendix. The mean model of the GPR then captures most of the HF response by linear transfer-learning of the LF model, leaving the remaining nonparametric approximation for the residual via a Gaussian process whose kernel hyperparameters are optimized as usual (Step 2.2 in Algorithm 1). The resulting KRR-LR-GPR model predicts the response and corresponding uncertainty, usually by following a Normal distribution $\mathcal{N}(\hat{f}^h(\mathbf{x}), \hat{s}_{\hat{f}^h}^2(\mathbf{x}))$ to ensure fast training and inference (exact integration of posterior and posterior predictive distributions). We find that a first-order linear transfer-learning model including a bias term, i.e. $\mathbf{m}(\mathbf{x}) = [1, f^l(\mathbf{x})]^T$, provides robust results according to the ablation study for different problems (see Appendix E.1).

Algorithm 1: KRR-LR-GPR

Data: LF dataset $\mathcal{D}(\mathbf{X}^l, \mathbf{y}^l)$, HF dataset $\mathcal{D}(\mathbf{X}^h, \mathbf{y}^h)$

Result: $\mathcal{N}(\hat{f}^h(\mathbf{x}), \hat{s}_{\hat{f}^h}^2(\mathbf{x}))$

Step 1: Train $f^l(\mathbf{x})$ by optimizing θ^l based on LF dataset $\mathcal{D}(\mathbf{X}^l, \mathbf{y}^l)$

Step 2: Train $g(\mathbf{x})$ and $r(\mathbf{x})$ based on $\mathcal{D}(\mathbf{X}^h, \mathbf{y}^h)$ and $f^l(\mathbf{x})$

Step 2.1: Calculate $\hat{\rho} = (\mathbf{m}(\mathbf{X}^h)\mathbf{K}(\mathbf{X}^h, \mathbf{X}^h)^{-1}\mathbf{m}(\mathbf{X}^h)^T)^{-1}\mathbf{m}(\mathbf{X}^h)\mathbf{K}(\mathbf{X}^h, \mathbf{X}^h)^{-1}\mathbf{y}^h$

Step 2.2: Optimize concentrated ln-likelihood function for θ^h

3.2 Model for data-rich or high-dimensional scenarios: DNN-LR-BNN

Pairing a DNN as the LF model with a BNN in a MF model leverages the scalability of DNNs with the predictive abilities of BNNs. We propose two MF models of this type, and argue in favor of the simpler one. The simpler model summarized in Fig.2 is labeled DNN-LR-BNN, where transfer-learning is done via linear regression (LR) as in Eq. (4), and the residual is modeled by a BNN. This can be interpreted as having the DNN in parallel with the BNN but doing a linear transformation of the DNN to the HF data before training the BNN. A more expressive and more flexible MF model is to avoid LR and just consider DNN-BNN, i.e. doing transfer-learning directly with a BNN on the HF data and disregarding the residual as in Eq. (3).

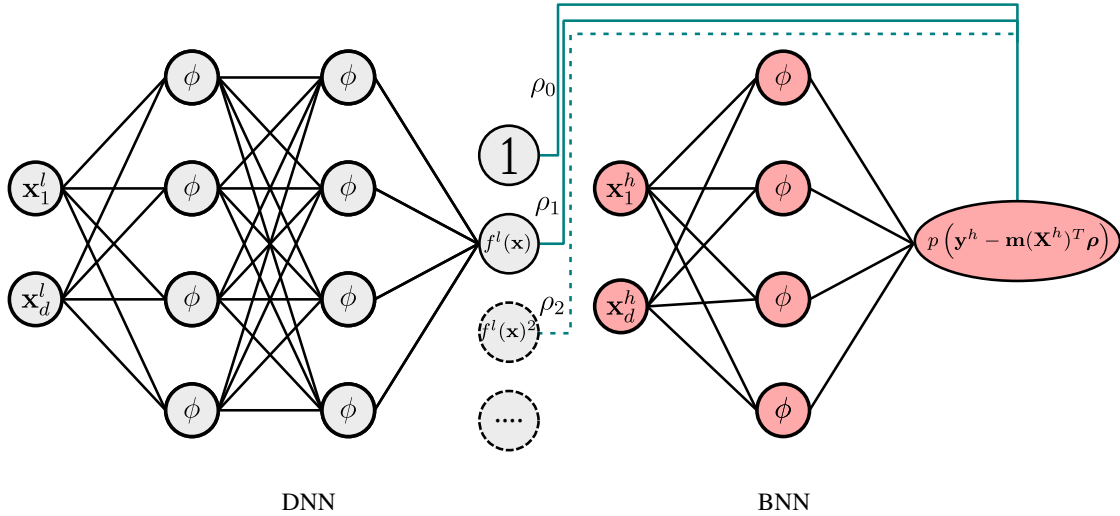


Figure 2: Schematic of the DNN-LR-BNN architecture. The DNN is trained on LF data, then it is used as a basis function of a linear transfer-learning model g that better explains the HF data and that is represented by the green connections, leading to $\mathbf{m}(\mathbf{x}^h)^T \boldsymbol{\rho}$. The BNN is then trained on the residual $r(\mathbf{x}^h) = \mathbf{y}^h - \mathbf{m}(\mathbf{x}^h)^T \boldsymbol{\rho}$.

In the DNN-LR-BNN model, the BNN models the residual as $r(\mathbf{x}^h) = \mathbf{y}^h - \mathbf{m}(\mathbf{x}^h)^T \boldsymbol{\rho}$, where the order of the basis $\mathbf{m}(\mathbf{x}^h)$ is a hyperparameter that can be determined by cross-validation or hyperparameter optimization, similarly to the previously mentioned KRR-LR-GPR model. The most common prior assumed for BNNs is the Normal distribution and this choice also leads to the same distribution for the DNN-LR-BNN architecture because $r(\mathbf{x})$ converges to standard

Normal distribution when the LF and HF models are highly correlated. There are many viable strategies for inference in BNNs, as reviewed previously: from Markov Chain Monte Carlo approaches like Hamiltonian Monte Carlo [52, 53] to Stochastic Gradient Langevin Dynamics (SGLD) [48], passing through Variational Inference approaches such as Bayes by Back-propagation [49], etc. In practice, for large datasets we recommend the use of a variant of SGLD called pSGLD [58] due to its superior scalability [59] – additional details are provided in Appendix A.1.1.

Contrary to the KRR-LR-GPR model, the determination of the transfer-learning parameters ρ is not done by Eq. (24) because it becomes intractable to calculate the covariance matrix of a BNN. Simultaneously, using cross-validation or other hyperparameter tuning strategies can be computationally intensive due to the time needed for BNN inference. Therefore, we propose to estimate ρ by solving the following optimization problem before training the BNN:

$$\min_{\rho} \sum_{i=1}^{N^h} \left(\mathbf{y}^h - \mathbf{m}(\mathbf{X}^h)^T \rho \right) \quad (8)$$

This equation is easy to optimize, akin to what is done in linear regression. Also, recall that by assuming $\rho_0 = 0$ and $\rho_1 = 1$, we obtain a vanilla MF model that fuses a DNN with a BNN without additional parameters. In summary, the main steps of DNN-LR-BNN are listed in Algorithm 2, leading to a Normal distribution prediction $\mathcal{N}(\hat{f}^h(\mathbf{x}), \hat{s}_{\hat{f}^h}^2(\mathbf{x}))$ at any unknown point.

Algorithm 2: DNN-LR-BNN

Data: LF dataset $\mathcal{D}(\mathbf{X}^l, \mathbf{y}^l)$, HF dataset $\mathcal{D}(\mathbf{X}^h, \mathbf{y}^h)$

Result: $\mathcal{N}(\hat{f}^h(\mathbf{x}), \hat{s}_{\hat{f}^h}^2(\mathbf{x}))$

Step 1: Train DNN based on LF dataset $\mathcal{D}(\mathbf{X}^l, \mathbf{y}^l)$ and corresponding DNN settings

Step 2: Train $g(\mathbf{x})$ and $r(\mathbf{x})$ based on $\mathcal{D}(\mathbf{X}^h, \mathbf{y}^h)$ and $f^l(\mathbf{x})$

Step 2.1: Obtain ρ by minimizing $\sum_{i=1}^{N^h} \left(\mathbf{y}^h - \mathbf{m}(\mathbf{X}^h)^T \rho \right)$

Step 2.2: BNN inference with pSGLD

4 Experiments

We analyze the performance of KRR-LR-GPR, DNN-LR-BNN and DNN-BNN models separately and compare them with state-of-the-art strategies. For comparison with the KRR-LR-GPR method, we select Co-Kriging [16], Hierarchical Kriging [23], and Scaled Kriging [26]. We consider 10 different functions to be learned using datasets with two fidelities, as described in Appendix C.1. These are low-dimensional functions with an input dimension spanning from $d = 1$ to $d = 8$, so they only need a small number of HF training samples. Importantly, the datasets utilized in this section are assumed to be noisy². Additional experiments are conducted in Appendix D where noiseless datasets are also considered. Concerning the performance assessment of DNN-LR-BNN, comparison with other models is more challenging due to the multitude of hyperparameters and model choices that are possible when considering neural networks in different fidelities. Therefore, we compare DNN-LR-BNN with single-fidelity BNN and DNN-BNN models considering the same hyperparameters, as summarized in Appendix F. Several different numerical examples are considered.

Regarding the accuracy metrics, no single metric can objectively evaluate model performance for comparison. To this end, we considered Normalized Root Mean Square Error (NRMSE) and R2 Score to assess the global predictive mean performance, calculated based on the noiseless ground truth and predictive mean [60]. Concerning the uncertainty quantification metric, we adopted the Test Log-Likelihood (TLL) calculated based on the noisy test dataset [61]. In addition, the CPU execution time for LF and HF are recorded to evaluate computational efficiency, and each experiment is conducted on a node of an HPC cluster platform with an Intel® Xeon(R) E5-2643v3 CPU with 6 cores of 3.40GHz and 128 GB of RAM.

4.1 Experiments with data-scarce HF and low-dimensional problems: KRR-LR-GPR

4.1.1 Illustrative example

Given the traditional importance of the Forrester function [16, 23], we start by illustrating the effectiveness of the KRR-LR-GPR method on this function – see Eq. (28) – and comparing it with alternative formulations seen in the

²We implemented the existing methods such that noisy datasets could also be considered.

literature that involve GPR models for both fidelities. We start by sampling 7 and 200 samples uniformly for HF and LF, respectively, and added Gaussian noise $\mathcal{N}(0, 0.3^2)$ on both LF and HF. However, our investigation later also considers different sample sizes and different noise levels. Fig.3 shows the results for all three MF-GPR models compared to the proposed KRR-LR-GPR model of an arbitrary realization.

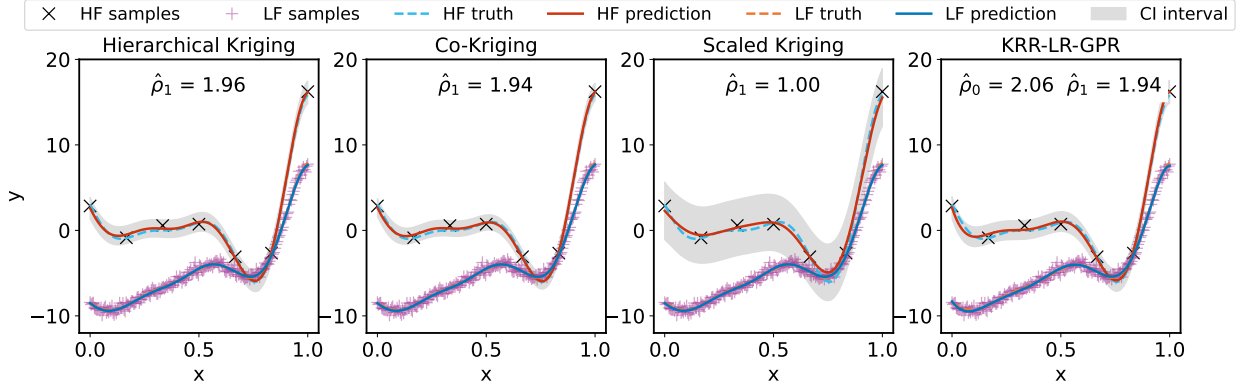


Figure 3: Fitting performance of KRR-LR-GPR on the illustrative example.

Table 2: Performance comparison between KRR-LR-GPR and other MF-GPR methods on the illustrative example

Methods	NRMSE	R2 Score	TLL	$\hat{\sigma}_h$	LF training time (s)	HF training time (s)
Hierarchical Kriging	0.0912	0.9971	-0.5771	0.3610	4.6584	0.2015
Co-Kriging	0.0862	0.9974	-0.4991	0.3505	8.0879	0.3257
Scaled Kriging	0.2163	0.9842	-1.4960	1.1989	5.8713	0.2847
KRR-LR-GPR	0.1232	0.9949	-0.6676	0.4440	3.5073	0.1986

The Forrester function is easily predicted by all methods, except Scaled Kriging that exhibits lower performance. Note that the HF predictive means almost overlap perfectly with the HF truth with NRMSE approaching zero and R2 Score close to 1 in Table 2. Co-Kriging, Hierarchical Kriging, and KRR-LR-GPR all converge to similar $\hat{\rho}_1$, that is different from the imposed value of $\hat{\rho}_1 = 1$ for Scaled Kriging – affecting its performance. Notwithstanding, even this simple example already shows that the KRR-LR-GPR requires less training time than other MF-GPR approaches, due to the use of kernel ridge regression for the LF.

We then investigated the influence of imposing different correlations between the LF and HF data, as shown in Eq. (29), for the proposed KRR-LR-GPR method. Fig.4 presents the trained KRR-LR-GPR model considering different LF datasets. Three different LF functions are used to generate three different LF datasets, so the figures are labeled as “LF data 1”, “LF data 2” and “LF data 3” accordingly. Table 3 summarizes the performance of the KRR-LR-GPR model.

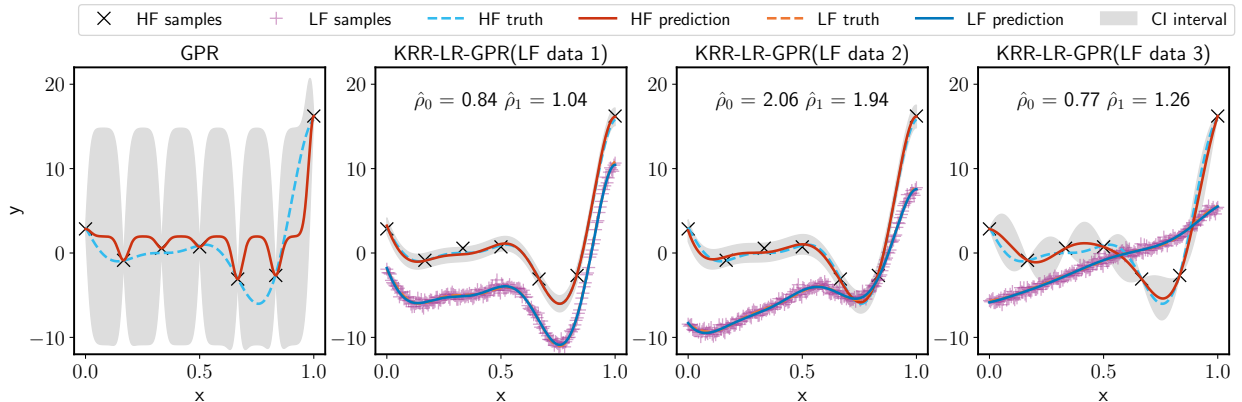


Figure 4: Predictions of KRR-LR-GPR for the Forrester function with different LF datasets of decreasing correlation (from left to right), as indicated in Table 3. The figure on the left corresponds to the single-fidelity result of GPR.

Table 3: Results comparison of the illustrative example with different LF datasets

Methods	KRR-LR-GPR			
	GPR	LF data 1	LF data 2	LF data 3
Pearson cor. coef. r	-	1.0	0.737	0.407
NRMSE	1.3129	0.0724	0.1226	0.2971
R2 Score	0.4188	0.9982	0.9949	0.9702
TLL	-18513.24	-0.4253	-0.6637	-19161.03
hf training time (s)	0.1175	0.1635	0.1833	0.1080
lf training time (s)	-	3.6946	4.3618	4.4272
$\hat{\sigma}^h$	0.000064	0.3995	0.4411	0.000061

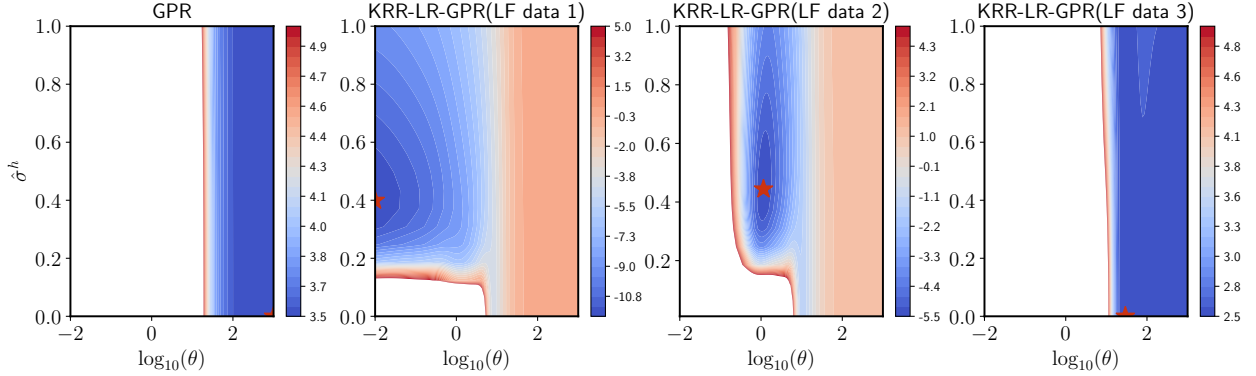


Figure 5: Negative log marginal likelihood values of GPR and KRR-LR-GPR within parameter space. The contour plots only show regions where the negative log marginal likelihood value is smaller than 5 for better illustration, the maximum values for each method are more than 10^7 . The X-axis represents kernel parameter $\log_{10}(\theta)$ and the Y-axis is the estimated noise level $\hat{\sigma}^h$, the red point is the best parameter found for every method by "L-BFGS-B" with 10 restarts.

From Fig.5 and Table 3 we see that the single-fidelity GPR cannot learn the underlying function because it fails to identify the noise level. However, the LF of the KRR-LR-GPR conditions the residual of the GPR and leads to good predictions according to NRMSE and R2 Score evaluated. Unsurprisingly, performance deteriorates as the Pearson correlation coefficient r between the two fidelities decreases from LF data 1 to 3. In terms of the estimated HF noise standard deviations, they are 0.3995, 0.4411, and 0.000061, respectively. This can be understood by observing Fig.5 that shows the landscape of negative log marginal likelihood values in the parameter space for the three cases, where it is highlighted that in the third case there is no a clear optimum value (right most figure) and the marginal likelihood is more similar to the single fidelity GPR model (left most figure) – this explains why the noise level at the HF is not properly estimated. The results are intuitive and explainable: if the LF data has limited or nonexistent correlation with the HF, then the predictive capability of the MF model degrades.

Table 4: Results of KRR-LR-GPR on Forrester function with different LF samples and noise levels

LF samples	σ_a^l	NRMSE	R2 Score	TLL	$\hat{\sigma}^h$
11	0.0	0.0858	0.9975	-0.4811	0.2741
	0.3	0.1971	0.9869	-0.9940	0.6089
	0.5	0.3056	0.9685	-1.3586	0.9187
	1.0	1.2941	0.4353	-47601.48	0.000061
200	0.0	0.0839	0.9976	-0.4715	0.2698
	0.3	0.0815	0.9977	-0.4768	0.2428
	0.5	0.0908	0.9972	-0.5523	0.2309
	1.0	0.1355	0.9938	-0.7897	0.2597

re, we also investigate the performance of the KRR-LR-GPR model with different noise levels (see Fig.6 and Table 4). We consider different Gaussian noise for the LF with standard deviations of $\sigma^l = 0.0$, $\sigma^l = 0.3$, $\sigma^l = 0.5$, and $\sigma^l = 1.0$, such that the robustness of KRR-LR-GPR to LF noise is reported while keeping the HF noise as $\sigma^h = 0.3$. The figure

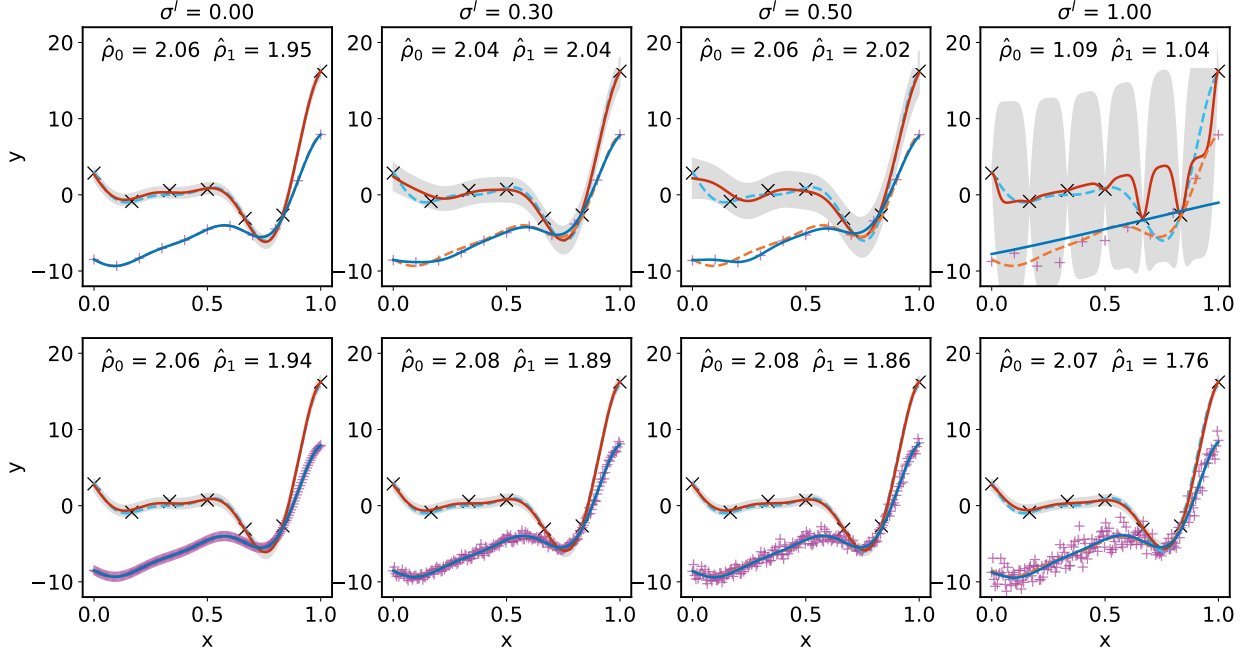


Figure 6: Performance of KRR-LR-GPR on Forrester function with different LF samples and noise levels: the top and bottom rows have 11 and 200 LF samples, respectively, while all cases consider 7 HF samples. Noise level of LF indicated by σ^l and number of LF samples is clear from the cross markers in each plot.

and table clarify that the model predicts both the function and noise level accurately for the cases with enough LF data. Conversely, it struggles to identify proper noise levels in cases of 11 LF points and higher LF noise levels, as expected.

4.1.2 Comprehensive experiments of KRR-LR-GPR

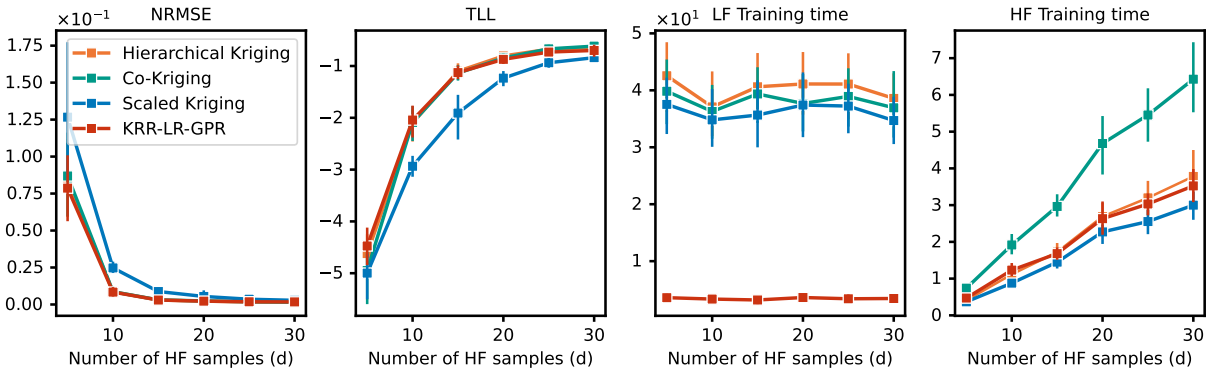


Figure 7: Comparison of KRR-LR-GPR with state-of-the-art MF methods for different sizes of HF datasets (here showing results for the Booth function, $d = 2$, Pearson cor. coef. $r = 0.925$). Different colors represent different methods. To interpret the results, note that a smaller NRMSE or a higher TLL is better. Note the significantly faster LF training time for KRR-LR-GPR compared to others.

Considering 10 analytical functions, we train them for the previously mentioned methods and report statistical results by repeating every experiment with 10 random initializations of the hyperparameters. Two experiments are conducted to benchmark the effectiveness and efficiency of the developed KRR-LR-GPR. All 10 functions lead to similar conclusions; therefore, we arbitrarily select the *Booth* function for demonstration (results of other functions are reported in Appendix D.1). Fig.7 shows the results assuming a fixed number of LF samples ($200 \times d$ where d is the dimension of the particular function being trained), and then consider a different number of HF samples (from $5 \times d$ to $30 \times d$). Fig. 8 pertains to a

different experiment where we fix the number of HF samples to $20 \times d$, and consider different number of LF samples (from $50 \times d$ to $300 \times d$). Moreover, Gaussian noise with standard deviations of $\sigma^l = 0.3$ and $\sigma^h = 0.3$ is considered for the datasets in both cases.

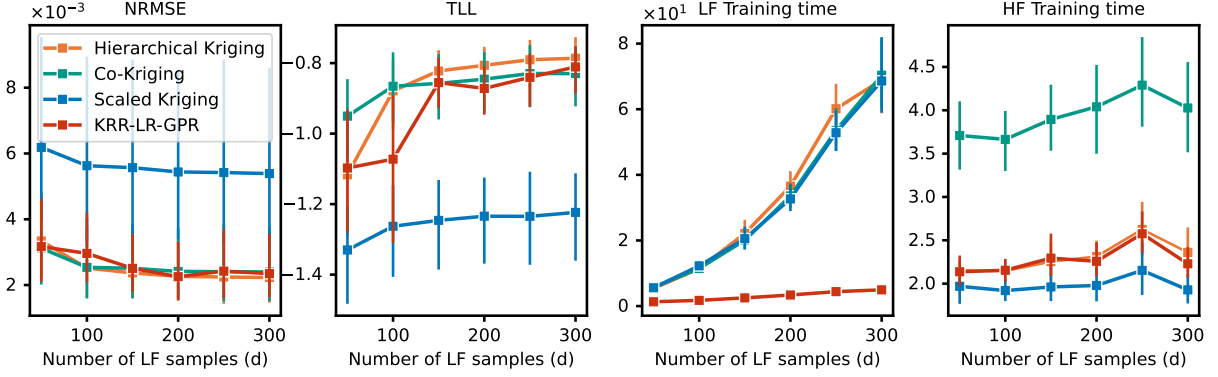


Figure 8: Comparison of KRR-LR-GPR with state-of-the-art methods considering different sizes of the LF dataset (Booth function, $d = 2$, Pearson cor. coef. $r = 0.925$).

The figures reinforce the argument that considering KRR for the LF and GPR for the residual creates a MF model with comparable performance to considering a GPR for all fidelities (hierarchically or not), while the computational cost decreases dramatically. Essentially, the computational complexity is reduced to $\mathcal{O}((N^h)^3 + (N^l)^2)$ instead of $\mathcal{O}((N^h + N^l)^3)$. For cases where the HF training data is scarce and low dimensional, we recommend to use a Bayesian method like GPR for that fidelity and a scalable method like KRR for the LF.

4.2 Experiments with data-rich HF and high-dimensional problems: DNN-LR-BNN

4.2.1 Illustrative example

We start with a one-dimensional illustrative example (data-scarce and low-dimensional) with 11 HF samples and 201 LF samples distributed uniformly. Aiming at explaining the limitations of the different MF models with DNNs and BNNs, we select three different LF datasets, labeled as “LF data 1”, “LF data 2” and “LF data 3”, obtained by considering different transformations of the HF data according to Eq. (50). Model performance and accuracy metrics are shown in Fig. 9 and Table 5. Table 5 also includes the different Pearson correlation coefficients (r) between LF and HF data. The figure includes the single fidelity BNN prediction at the top left.

Table 5: Results comparison of DNN-LR-BNN on the 1D noisy illustrative example

LF Dataset	Methods	NRMSE	R2 Score	TLL
—	BNN	1.0925	-0.8377	-4.5359
LF Data 1 ($r = -0.1019$)	DNN-BNN	0.2102	0.9319	0.7982
	DNN-LR ¹ -BNN	1.0431	-0.6755	-7.7032
	DNN-LR ² -BNN	0.3196	0.8426	0.4925
LF Data 2 ($r = 0.9999$)	DNN-BNN	0.2234	0.9230	1.0007
	DNN-LR ¹ -BNN	0.0854	0.9887	1.4982
LF Data 3 ($r = -0.0018$)	DNN-BNN	1.3933	-1.9895	-4.7059
	DNN-LR ¹ -BNN	1.0607	-0.7326	-5.1139

* The subscripts 1 and 2 indicate different LF basis function orders utilized by the linear regression (LR) transfer learning model.

Fig. 9 and Table 5 illustrate that if LF and HF data are not linearly correlated (as in “LF data 1” and “LF data 3” examples), then considering linear regression with first-order terms to do transfer learning between the DNN and BNN leads to a prediction by the DNN-LR-BNN model that becomes similar to the single-fidelity BNN prediction. This directly results from the LR transfer-learning model determining a low correlation (parameter ρ_1 becomes close to

zero). We believe that this is a strength of the proposed strategy because it automatically informs the analyst about the correlation between LF and HF data, suppressing the LF influence on the HF prediction when this correlation does not exist, favoring more parsimonious models (closer to the single-fidelity BNN). We also include an example of a quadratic LR transfer-learning model for the “LF data 1” example, labeled as DNN-LR²-BNN, where we show that the performance improves significantly when compared to a first-order LR model (labeled as “DNN-LR¹-BNN”). Evidently, if LF and HF data become better correlated (as in “LF data 2” example), the DNN-LR-BNN model tends to have better performance.

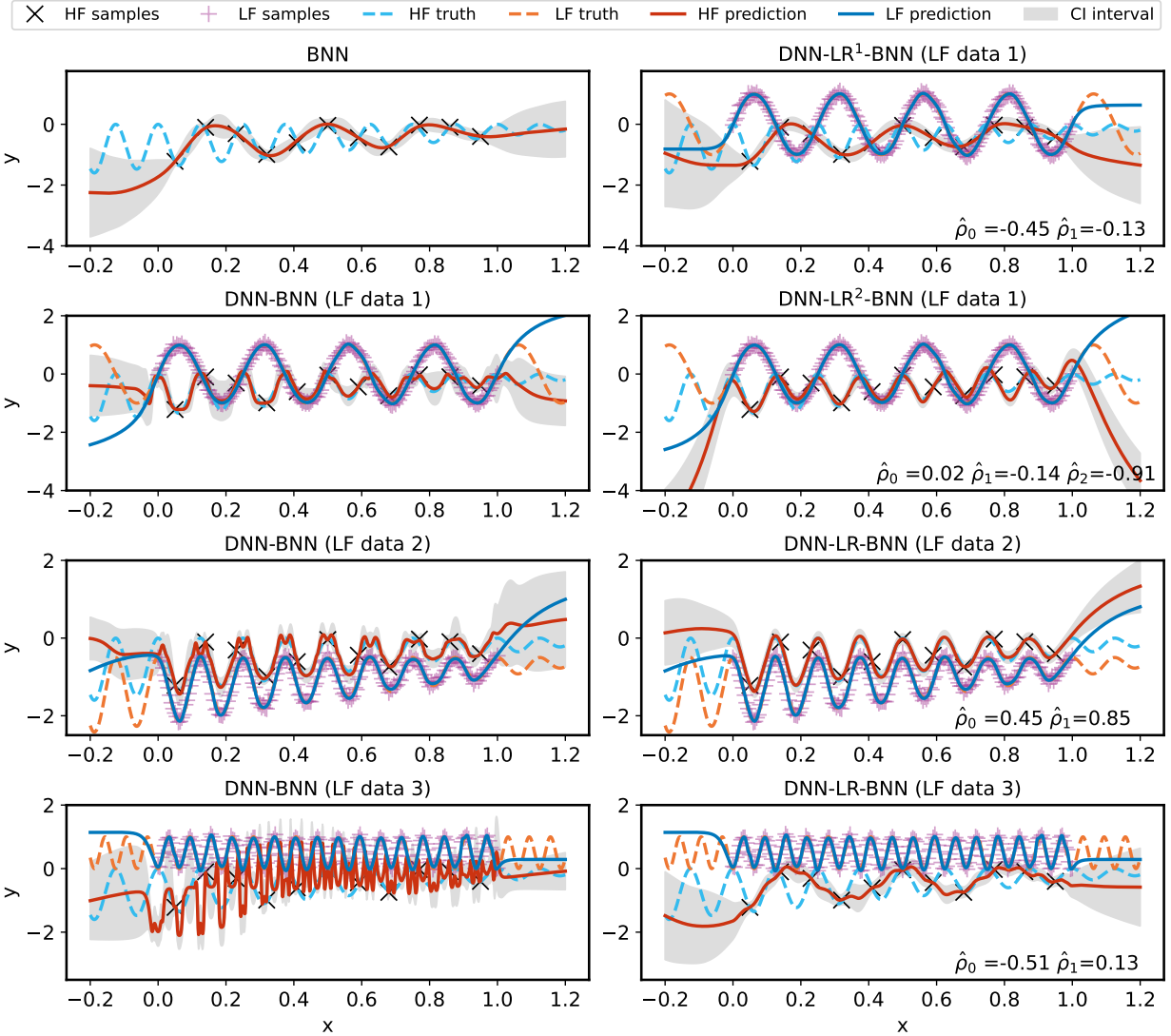


Figure 9: One-dimensional illustrative example comparing the proposed DNN-LR-BNN method (right column) with a BNN trained exclusively with HF data, and with a simple DNN-BNN (left column). Three LF datasets are employed whose Person correlation coefficients are -0.1019 , 0.9999 , and -0.0018 correspondingly.

In addition, we want to highlight that being tempted to use the most flexible model, i.e. DNN-BNN, also has disadvantages as it tends to a less parsimonious model that risks overfitting (see bottom left of Fig. 9). This can be dangerous in the context of multi-fidelity because the LF often includes random and systematic errors that disrupt the HF predictions. Hence, the early literature in multi-fidelity considered first-order linear relationships between LF and HF models governed by a single hyperparameter (ρ_1). In general, however, performing model selection and establishing a simple (but not simpler) transfer-learning model between the DNN and BNN is a key consideration in practice.

We also want to bring to the reader’s attention that neural network training is highly dependent on architectural and hyperparametric choices. Appendix F.2 details the dependence on hyperparameters and reinforces that the DNN-LR-

BNN model is simpler to train and is less sensitive to hyperparameter choices than the more flexible DNN-BNN model. We observed in all cases that the prediction of uncertainty depends on the width of the BNN, i.e. on the number of neurons in the hidden layers. A wide network tends to the same uncertainty prediction obtained by GPR, while the prediction of the expected value (the mean) converges even for shallower BNNs.

4.2.2 Higher dimensional examples

We also demonstrate the performance of DNN-LR-BNN and DNN-BNN in problems with higher dimensions and larger datasets. We consider two functions, a 4-dimensional function extracted from [13] and another function from [43] where we set the dimension to be [20, 50, 100] in this subsection. The results are summarized in Table 6.

Table 6: Results comparison of DNN-LR-BNN on the high-dimensional examples

Dimension	Methods	NRMSE	R2 Score	TLL	$\hat{\rho}_0$	$\hat{\rho}_1$
4	BNN	0.7624 (± 0.031)	-0.6296 (0.131)	-5.3555 (± 0.458)	-	-
	DNN-BNN	0.1163 (± 0.013)	0.9617 (± 0.009)	1.2680 (± 0.040)	-	-
	DNN-LR ¹ -BNN	0.0777 (± 0.013)	0.9826 (± 0.006)	1.4090 (± 0.045)	-0.41 (± 0.002)	0.86 3(± 0.006)
20	BNN	0.1598 (± 0.004)	0.7418 (± 0.013)	-23.5060 (± 1.673)	-	-
	DNN-BNN	0.0723 (± 0.010)	0.9463 (± 0.015)	-8.1125 (± 1.137)	-	-
	DNN-LR ¹ -BNN	0.0662 (± 0.008)	0.9550 (± 0.012)	-8.7991 (± 0.905)	55.75 (± 17.091)	1.26 (± 0.005)
50	BNN	0.1725 (± 0.003)	0.2341 (± 0.024)	-59.2736 (± 3.671)	-	-
	DNN-BNN	0.0879 (± 0.001)	0.8008 (± 0.007)	-17.7602 (± 0.9644)	-	-
	DNN-LR ¹ -BNN	0.0851 (± 0.001)	0.8137 (± 0.003)	-17.3543 ($\pm 0.0.8955$)	62.0892 (± 5.219)	1.2504 (± 0.001)
100	BNN	0.1343 (± 0.001)	0.0564 (± 0.020)	-113.4960 (± 8.007)	-	-
	DNN-BNN	0.0867 (± 0.002)	0.6062 (± 0.018)	-58.8356 (± 6.7228)	-	-
	DNN-LR ¹ -BNN	0.0845 (± 0.001)	0.6265 (± 0.008)	-58.7305 (± 4.458)	-100.0 (± 0.0)	1.2868 (± 0.013)

Table 6 shows that the single fidelity BNN leads to poor predictions for all examples according to all accuracy metrics. Also for all cases, the DNN-LR-BNN outperforms DNN-BNN. For the 4D function, unsurprisingly, the learned parameters $\hat{\rho}_0 = 0.86$ and $\hat{\rho}_1 = -0.41$ are very close to the ground-truth $\rho_0 = 0.83$ and $\rho_1 = -0.33$ showed in Eq. (55).

5 Discussion and limitations

Expressive machine learning algorithms typically have limited extrapolation ability because their large number of parameters is used to explain the training data without necessarily discovering the underlying functional form that explains the data. DNNs often make unreliable predictions for points away from sampled points; conversely, Bayesian models such as GPRs and BNNs eventually reverse to the prior [62]. A similar issue also occurs in the DNN-BNN architecture where the HF prediction is distorted in the unsampled region as reported in Fig. 10. However, KRR-LR-GPR and DNN-LR-BNN alleviate this shortcoming to some degree because they remain smooth and close to the HF truth. The proposed transfer-learning model in Eq. (4) narrows the gap between $\mathbf{m}(\mathbf{X}^h)^T \boldsymbol{\rho}$ and \mathbf{y}^h , while the BNN captures the residual utilizing a prior with zero mean that reverses to another constant after training (see purple line in Fig. 10). Therefore, the HF prediction is influenced by the parsimonious (simple) transfer-learning model, having higher chances of reasonable extrapolation.

However, when we compare the DNN-LR-BNN model prediction with the KRR-LR-GPR one, we see that although the mean is similar, the uncertainty prediction is not. The DNN-LR-BNN uncertainty is smaller at the extrapolation

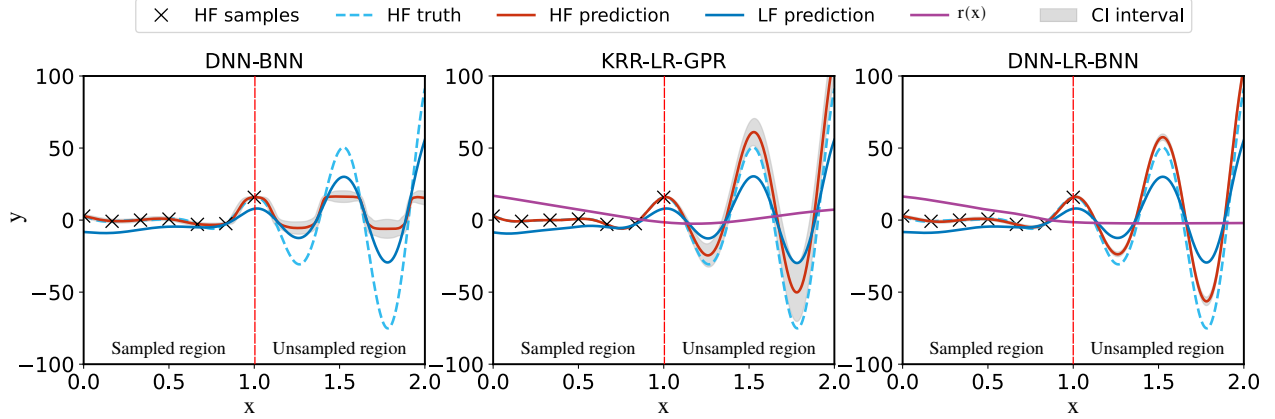


Figure 10: Equivalence of KRR-LR-GPR and DNN-LR-BNN: The LF samples locate from zero to two while the HF samples stay in the region between zero and one

region, demonstrating the model is overconfident. We identify two reasons for this observation. First, the inference of the BNN is approximate and does not yield the exact posterior predictive distribution. This bottleneck can be resolved for a specific problem by fine-tuning the hyperparameters of BNN using test data or cross-validation, increasing the number of neurons in the hidden layers, as previously shown. Second, there is an inherent bottleneck in evaluating uncertainty via Eq. (16) when a BNN is employed for $f^h(\mathbf{x})$ inference: the covariance matrix $\mathbf{K}(\mathbf{X}, \mathbf{X})$ is difficult to compute and so the uncertainty present in the LF model is difficult to transport to the HF prediction.

6 Conclusions

In this study, we created a general multi-fidelity framework that encompasses different multi-fidelity strategies in the literature. We propose using non-probabilistic LF models together with Bayesian HF models, and recommend two practical strategies to deal with data-scarce and data-rich scenarios. For the first case, we propose the the KRR-LR-GPR multi-fidelity model that considers kernel ridge regression for LF, linear regression for transfer learning data from LF to HF, and Gaussian process regression for modeling the residual that remains. For data-rich and high-dimensional cases, we recommend the use of DNN-LR-BNN that considers deep neural network for LF, linear regression transfer-learning, and Bayesian neural network for the residual. In case a linear regression model does not provide an effective transfer learning method, a more flexible DNN-BNN model is recommended using pSGLD as inference method for high-dimensional datasets.

The KRR-LR-GPR model is assessed for cases with and without noise for both fidelities and its performance is similar to the best state-of-the-art multi-fidelity GPR approaches, while having significantly shorter inference time (the KRR-LR-GPR method becomes bounded only by the number of HF samples). Finally, an ablation study shows the performance of KRR-LR-GPR is influenced by factors similar to those of other multi-fidelity GPR methods, so the observations align with those discussed in [8] for those methods.

We also report the performance of the DNN-LR-BNN compared with that of a single-fidelity BNN and a flexible multi-fidelity model considering only DNN-BNN. We observed that DNN-LR-BNN has lower tendency to overfit than DNN-BNN, as the LR transfer-learning model isolates the HF from the LF when they are not linearly correlated. Furthermore, we highlight the proposed strategy to determine ρ from training, instead of considering them as hyperparameters as in the literature.

Although the DNN-LR-BNN model can converge to the results of the KRR-LR-BNN model for cases when both are applicable, the KRR-LR-GPR model is easier to train because it has significantly fewer hyperparameters, hence the motivation of recommending it for data-scarce or lower dimensional scenarios.

Data availability

The code is available on: <https://github.com/bessagroup/mfbml>

Declaration of Generative AI and AI-assisted technologies in the writing process

The first author used CHATGPT and GRAMMARLY to IMPROVE LANGUAGE AND READABILITY. After using these tools/services, the authors reviewed and edited the content as needed and assume full responsibility for the content of the publication.

Acknowledgments

Jiaxiang Yi would like to acknowledge the generous support of the China Scholarship Council (CSC).

References

- [1] Kurt Hornik, Maxwell Stinchcombe, and Halbert White. Multilayer feedforward networks are universal approximators. *Neural Networks*, 2(5):359–366, 1989.
- [2] Chiyuan Zhang, Samy Bengio, Moritz Hardt, Benjamin Recht, and Oriol Vinyals. Understanding deep learning (still) requires rethinking generalization. *Commun. ACM*, 64(3):107–115, feb 2021.
- [3] Nicholas G. Polson and Vadim Sokolov. Deep learning: A bayesian perspective. *Bayesian Analysis*, 12(4), dec 2017.
- [4] Jie Chen, Changyu Meng, Yi Gao, and Yongming Liu. Multi-fidelity neural optimization machine for digital twins. *Structural and Multidisciplinary Optimization*, 65(12):340, 2022.
- [5] Qi Zhou, Jinhong Wu, Tao Xue, and Peng Jin. A two-stage adaptive multi-fidelity surrogate model-assisted multi-objective genetic algorithm for computationally expensive problems. *Engineering with Computers*, 37(1):623–639, 2021.
- [6] Zeliang Liu, M.A. Bessa, and Wing Kam Liu. Self-consistent clustering analysis: An efficient multi-scale scheme for inelastic heterogeneous materials. *Computer Methods in Applied Mechanics and Engineering*, 306:319–341, 2016.
- [7] Xinshuai Zhang, Fangfang Xie, Tingwei Ji, Zaoxu Zhu, and Yao Zheng. Multi-fidelity deep neural network surrogate model for aerodynamic shape optimization. *Computer Methods in Applied Mechanics and Engineering*, 373:113485, 2021.
- [8] David J. J. Toal. Some considerations regarding the use of multi-fidelity kriging in the construction of surrogate models. *Structural and Multidisciplinary Optimization*, 51(6):1223–1245, 2015.
- [9] M. Giselle Fernández-Godino, Chanyoung Park, Nam H. Kim, and Raphael T. Haftka. Issues in deciding whether to use multifidelity surrogates. *AIAA Journal*, 57(5):2039–2054, 2019.
- [10] M. Giselle Fernández-Godino. Review of multi-fidelity models. *Advances in Computational Science and Engineering*, 1(4):351–400, 2023.
- [11] Haitao Liu, Jianfei Cai, and Yew-Soon Ong. Remarks on multi-output gaussian process regression. *Knowledge-Based Systems*, 144:102–121, 2018.
- [12] Kurt Cutajar, Mark Pullin, Andreas Damianou, Neil Lawrence, and Javier González. Deep gaussian processes for multi-fidelity modeling, 2019.
- [13] Xuhui Meng, Hessam Babae, and George Em Karniadakis. Multi-fidelity bayesian neural networks: Algorithms and applications. *Journal of Computational Physics*, 438:110361, 2021.
- [14] Carl Edward Rasmussen and Christopher K. I. Williams. *Gaussian Processes for Machine Learning*. The MIT Press, 11 2006.
- [15] Marc C Kennedy and Anthony O’Hagan. Predicting the output from a complex computer code when fast approximations are available. *Biometrika*, 87(1):1–13, 2000.
- [16] Alexander I.J Forrester, András Sóbester, and Andy J Keane. Multi-fidelity optimization via surrogate modelling. *Proceedings of the Royal Society A: Mathematical, Physical and Engineering Sciences*, 463(2088):3251–3269, 2007.
- [17] Quan Lin, Jiachang Qian, Yuansheng Cheng, Qi Zhou, and Jiexiang Hu. A multi-output multi-fidelity gaussian process model for non-hierarchical low-fidelity data fusion. *Knowledge-Based Systems*, 254:109645, 2022.
- [18] Jonathan Tammer Eweis-Labolle, Nicholas Oune, and Ramin Bostanabad. Data Fusion With Latent Map Gaussian Processes. *Journal of Mechanical Design*, 144(9), 06 2022. 091703.
- [19] Nicholas Oune and Ramin Bostanabad. Latent map gaussian processes for mixed variable metamodeling. *Computer Methods in Applied Mechanics and Engineering*, 387:114128, 2021.
- [20] Robert B. Gramacy. *Surrogates: Gaussian Process Modeling, Design and Optimization for the Applied Sciences*. Chapman Hall/CRC, Boca Raton, Florida, 2020. <http://bobby.gramacy.com/surrogates/>.
- [21] Haitao Liu, Jianfei Cai, and Yew-Soon Ong. Remarks on multi-output gaussian process regression. *Knowledge-Based Systems*, 144:102–121, 2018.
- [22] M. Giselle Fernández-Godino, Chanyoung Park, Nam H. Kim, and Raphael T. Haftka. Issues in deciding whether to use multifidelity surrogates. *AIAA Journal*, 57(5):2039–2054, 5 2019.
- [23] Zhong-Hua Han and Stefan Görtz. Hierarchical kriging model for variable-fidelity surrogate modeling. *AIAA Journal*, 50(9):1885–1896, 2012.

- [24] Zhong-Hua Han, Ralf Zimmermann, and Stefan Goretz. A new cokriging method for variable-fidelity surrogate modeling of aerodynamic data. In *48th AIAA Aerospace sciences meeting including the new horizons forum and Aerospace exposition*, page 1225, 2010.
- [25] Zhong-Hua Han, Stefan Görtz, and Ralf Zimmermann. Improving variable-fidelity surrogate modeling via gradient-enhanced kriging and a generalized hybrid bridge function. *Aerospace Science and Technology*, 25(1):177–189, 2013.
- [26] Chanyoung Park, Raphael T. Haftka, and Nam H. Kim. Low-fidelity scale factor improves bayesian multi-fidelity prediction by reducing bumpiness of discrepancy function. *Structural and Multidisciplinary Optimization*, 58(2):399–414, 2018.
- [27] Chanyoung Park, Nam Ho Kim, and Raphael T Haftka. Including ρ in multi-fidelity surrogate prediction can make discrepancy extrapolation accurate by reducing bumpiness. In *2018 AIAA/ASCE/AHS/ASC Structures, Structural Dynamics, and Materials Conference*, page 0915, 2018.
- [28] Loic Le Gratiet and Josselin Garnier. Recursive co-kriging model for design of computer experiments with multiple levels of fidelity. *International Journal for Uncertainty Quantification*, 4(5):365–386, 2014.
- [29] Haitao Liu, Yew-Soon Ong, Xiaobo Shen, and Jianfei Cai. When gaussian process meets big data: A review of scalable gps. *IEEE Transactions on Neural Networks and Learning Systems*, 31(11):4405–4423, 2020.
- [30] Dongxia Wu, Matteo Chinazzi, Alessandro Vespignani, Yi-An Ma, and Rose Yu. Multi-fidelity hierarchical neural processes. In *Proceedings of the 28th ACM SIGKDD Conference on Knowledge Discovery and Data Mining*. ACM, aug 2022.
- [31] Katerina Giannoukou, Stefano Marelli, and Bruno Sudret. A comprehensive framework for multi-fidelity surrogate modeling with noisy data: a gray-box perspective, 2024.
- [32] Yiming Zhang, Nam H. Kim, Chanyoung Park, and Raphael T. Haftka. Multifidelity surrogate based on single linear regression. *AIAA Journal*, 56(12):4944–4952, 2018.
- [33] Xueguan Song, Liye Lv, Wei Sun, and Jie Zhang. A radial basis function-based multi-fidelity surrogate model: exploring correlation between high-fidelity and low-fidelity models. *Structural and Multidisciplinary Optimization*, 60(3):965–981, 2019.
- [34] Maolin Shi, Liye Lv, Wei Sun, and Xueguan Song. A multi-fidelity surrogate model based on support vector regression. *Structural and Multidisciplinary Optimization*, 61(6):2363–2375, 2020.
- [35] Lucas Zimmer, Marius Lindauer, and Frank Hutter. Auto-pytorch: Multi-fidelity metalearning for efficient and robust autodl. *IEEE Transactions on Pattern Analysis and Machine Intelligence*, 43(9):3079–3090, 2021.
- [36] Dehao Liu and Yan Wang. Multi-Fidelity Physics-Constrained Neural Network and Its Application in Materials Modeling. *Journal of Mechanical Design*, 141(12), 09 2019. 121403.
- [37] Shibo Li, Wei Xing, Robert Kirby, and Shandian Zhe. Multi-fidelity bayesian optimization via deep neural networks. In H. Larochelle, M. Ranzato, R. Hadsell, M.F. Balcan, and H. Lin, editors, *Advances in Neural Information Processing Systems*, volume 33, pages 8521–8531. Curran Associates, Inc., 2020.
- [38] Mohammad Motamed. A multi-fidelity neural network surrogate sampling method for uncertainty quantification. *International Journal for Uncertainty Quantification*, 10(4):315–332, 2020.
- [39] Roland Can Aydin, Fabian Albert Braeu, and Christian Johannes Cyron. General multi-fidelity framework for training artificial neural networks with computational models. *Frontiers in Materials*, 6, 2019.
- [40] Souvik Chakraborty. Transfer learning based multi-fidelity physics informed deep neural network. *Journal of Computational Physics*, 426:109942, 2021.
- [41] Milan Papež and Anthony Quinn. Transferring model structure in bayesian transfer learning for gaussian process regression. *Knowledge-Based Systems*, 251:108875, 2022.
- [42] Nolan Black and Ahmad R. Najafi. Learning finite element convergence with the multi-fidelity graph neural network. *Computer Methods in Applied Mechanics and Engineering*, 397:115120, 2022.
- [43] Xuhui Meng and George Em Karniadakis. A composite neural network that learns from multi-fidelity data: Application to function approximation and inverse pde problems. *Journal of Computational Physics*, 401:109020, 2020.
- [44] Mengwu Guo, Andrea Manzoni, Maurice Amendt, Paolo Conti, and Jan S. Hesthaven. Multi-fidelity regression using artificial neural networks: Efficient approximation of parameter-dependent output quantities. *Computer Methods in Applied Mechanics and Engineering*, 389, 2022.

- [45] Paolo Conti, Mengwu Guo, Andrea Manzoni, and Jan S. Hesthaven. Multi-fidelity surrogate modeling using long short-term memory networks. *Computer Methods in Applied Mechanics and Engineering*, 404:115811, 2023.
- [46] Jinhong Wu, Xingxing Feng, Xuan Cai, Xufeng Huang, and Qi Zhou. A deep learning-based multi-fidelity optimization method for the design of acoustic metasurface. *Engineering with Computers*, 39(5):3421–3439, 2023.
- [47] Radford M Neal. *Bayesian learning for neural networks*, volume 118. Springer Science & Business Media, 1995.
- [48] Max Welling and Yee W Teh. Bayesian learning via stochastic gradient langevin dynamics. In *Proceedings of the 28th international conference on machine learning (ICML-11)*, pages 681–688, 2011.
- [49] Charles Blundell, Julien Cornebise, Koray Kavukcuoglu, and Daan Wierstra. Weight uncertainty in neural networks, 2015.
- [50] Yarin Gal and Zoubin Ghahramani. Dropout as a bayesian approximation: Representing model uncertainty in deep learning. In Maria Florina Balcan and Kilian Q. Weinberger, editors, *Proceedings of The 33rd International Conference on Machine Learning*, volume 48 of *Proceedings of Machine Learning Research*, pages 1050–1059, New York, New York, USA, 20–22 Jun 2016. PMLR.
- [51] Balaji Lakshminarayanan, Alexander Pritzel, and Charles Blundell. Simple and scalable predictive uncertainty estimation using deep ensembles. In I. Guyon, U. Von Luxburg, S. Bengio, H. Wallach, R. Fergus, S. Vishwanathan, and R. Garnett, editors, *Advances in Neural Information Processing Systems*, volume 30. Curran Associates, Inc., 2017.
- [52] Radford M Neal. Mcmc using hamiltonian dynamics. *Handbook of markov chain monte carlo*, 2(11):2, 2011.
- [53] Michael Betancourt. A conceptual introduction to hamiltonian monte carlo, 2018.
- [54] Baptiste Kerleguer, Claire Cannamela, and Josselin Garnier. A Bayesian neural network approach to Multi-fidelity surrogate modelling. working paper or preprint, March 2022.
- [55] Alexander Forrester, Andras Sobester, and Andy Keane. *Engineering design via surrogate modelling: a practical guide*. John Wiley & Sons, 2008.
- [56] Gil Shabat, Era Choshen, Dvir Ben Or, and Nadav Carmel. Fast and accurate gaussian kernel ridge regression using matrix decompositions for preconditioning. *SIAM Journal on Matrix Analysis and Applications*, 42(3):1073–1095, 2021.
- [57] Giacomo Meanti, Luigi Carratino, Lorenzo Rosasco, and Alessandro Rudi. Kernel methods through the roof: handling billions of points efficiently, 2020.
- [58] Chunyuan Li, Changyou Chen, David Carlson, and Lawrence Carin. Preconditioned stochastic gradient langevin dynamics for deep neural networks, 2015.
- [59] Wei Deng, Siqi Liang, Botao Hao, Guang Lin, and Faming Liang. Interacting contour stochastic gradient langevin dynamics, 2022.
- [60] Juyoung Lee, Mingyu Lee, Bong Jae Lee, and Ikjin Lee. A comprehensive multi-fidelity surrogate framework based on gaussian process for datasets with heterogeneous responses. *Knowledge-Based Systems*, 295:111827, 2024.
- [61] Sameer K. Deshpande, Soumya Ghosh, Tin D. Nguyen, and Tamara Broderick. Are you using test log-likelihood correctly?, 2024.
- [62] Steven Adriaensen, Herilalaina Rakotoarison, Samuel Müller, and Frank Hutter. Efficient bayesian learning curve extrapolation using prior-data fitted networks. In *Thirty-seventh Conference on Neural Information Processing Systems*, 2023.
- [63] Diederik P. Kingma and Jimmy Ba. Adam: A method for stochastic optimization, 2014.
- [64] Sebastian Ruder. An overview of gradient descent optimization algorithms, 2017.
- [65] Laurent Valentin Jospin, Hamid Laga, Farid Boussaid, Wray Buntine, and Mohammed Bennamoun. Hands-on bayesian neural networks—a tutorial for deep learning users. *IEEE Computational Intelligence Magazine*, 17(2):29–48, 2022.
- [66] Miles Cranmer. Interpretable machine learning for science with pysr and symbolicregression.jl, 2023.
- [67] S. Surjanovic and D. Bingham. Virtual library of simulation experiments: Test functions and datasets. Retrieved December 8, 2023, from <http://www.sfu.ca/~ssurjano>.
- [68] Ping Jiang, Ji Cheng, Qi Zhou, Leshi Shu, and Jiexiang Hu. Variable-fidelity lower confidence bounding approach for engineering optimization problems with expensive simulations. *AIAA Journal*, 57(12):5416–5430, 2019.

- [69] Sander van Rijn and Sebastian Schmitt. Mf2: A collection of multi-fidelity benchmark functions in python. *Journal of Open Source Software*, 5(52):2049, 2020.
- [70] L. Mainini, A. Serani, M. P. Rumpfkeil, E. Minisci, D. Quagliarella, H. Pehlivan, S. Yildiz, S. Ficini, R. Pellegrini, F. Di Fiore, D. Bryson, M. Nikbay, M. Diez, and P. Beran. Analytical benchmark problems for multifidelity optimization methods, 2022.

A Foundations of Bayesian machine learning

A.1 Bayesian neural networks

A regression problem can be defined by

$$\mathbf{y} = f(\mathbf{x}) + \epsilon \quad (9)$$

where ϵ is the data noise originating from the collecting process. In this paper, the data noise is assumed to be homoscedastic and obeys Normal distribution $\epsilon \sim \mathcal{N}(0, \sigma^2)$.

Consider first the nonprobabilistic DNNs. Fig.11a shows a DNN schematic, where the input \mathbf{x} passes through successive neurons located in hidden layers where nonlinear transformations $\phi(\mathbf{x})$ happen in so called activation functions. In the end, the prediction $\hat{\mathbf{y}}$ is outputted by the DNN and compared to the true data via loss function. The solid lines that connect neurons include parameters called weights \mathbf{w} while biases are not explicitly included in the schematic (together the weights and biases parameters are labeled as θ). These parameters are real values that are determined via optimization algorithms like Adam [63] and Stochastic Gradient Decent (SGD) [64] that minimize the loss function.

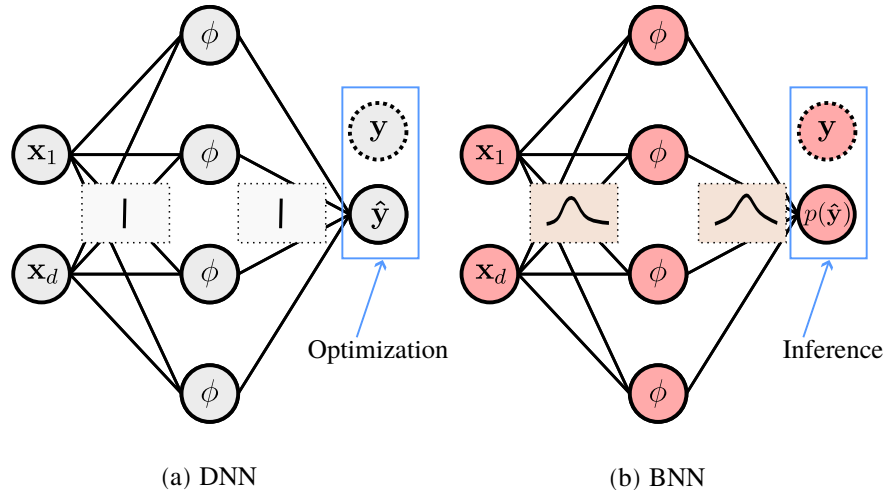


Figure 11: Schematics of DNN and BNN

BNNs are similar to DNNs, as shown in Fig.11b, but have a key difference: distributions over weights are considered instead of using a deterministic value as in DNNs. This probabilistic treatment allows BNNs to capture uncertainty in the predictions. Consequently, traditional optimization algorithms, suitable for finding point estimates, are not directly applicable to BNNs. The procedure to find the posterior parameter distribution is called inference, such that the posterior is determined as follows [47]:

$$p(\theta | \mathcal{D}) = \frac{p(\mathcal{D} | \theta)p(\theta)}{p(\mathcal{D})}, \quad p(\mathcal{D}) = \int p(\mathcal{D}, \theta)p(\theta) d\theta \quad (10)$$

where $p(\theta)$ is the prior, for example a normal distribution with θ containing the mean μ_w and standard deviation of the weights σ_w ; $p(\mathcal{D} | \theta)$ is the likelihood; $p(\mathcal{D})$ is the marginal likelihood or evidence, which is the probability integral of likelihood over θ ; and $p(\theta | \mathcal{D})$ is the posterior distribution of parameter θ . The aim when training BNNs is to maximize $p(\theta | \mathcal{D})$, although this is usually intractable because of the unbounded and complex probability integral. Therefore, methods such as Markov Chain Monte Carlo [47] and Variational Inference [49] are extensively used to determine an approximate posterior distribution. After obtaining parameters, the prediction for an unknown point is calculated by:

$$\hat{p}(\mathbf{y}' | \mathbf{x}', \mathcal{D}) = \int p(\mathbf{y}' | \mathbf{x}', \theta)p(\theta | \mathcal{D}) d\theta \quad (11)$$

where \mathbf{x}' is the location of the unknown point.

A.1.1 Bayesian inference method: pSGLD

As the analytical solution of the posterior predictive distribution of BNNs is intractable, we used preconditioned stochastic gradient Langevin dynamics (pSGLD) [58]. The posterior of a BNN can be regarded as $p(\theta | \mathcal{D}) \propto$

$p(\boldsymbol{\theta}) \prod_{n=1}^N p(y_i|\boldsymbol{\theta})$ according to Eq. (10), and we can define the update rule for the posterior as in SGLD [48]:

$$\Delta\boldsymbol{\theta}_t = \frac{\epsilon_t}{2} \left(\nabla \log p(\boldsymbol{\theta}_t) + \frac{N}{n} \log p(y_i|\boldsymbol{\theta}_t) \right) + \boldsymbol{\eta}_t \quad (12)$$

where $\boldsymbol{\eta}_t \sim \mathcal{N}(\mathbf{0}, \epsilon_t)$. However, SGLD assumes that all parameters $\boldsymbol{\theta}$ have the same step size, which can lead to slow convergence or even divergence in the cases where the components of $\boldsymbol{\theta}$ have different curvature. In pSGLD, the update rule incorporates a user-defined preconditioning matrix $G(\boldsymbol{\theta}_t)$, which adjusts the gradient updates and the noise term adaptively:

$$\Delta\boldsymbol{\theta}_t = \frac{\epsilon_t}{2} \left[G(\boldsymbol{\theta}_t) \left(\nabla \log p(\boldsymbol{\theta}_t) + \frac{N}{n} \log p(y_i|\boldsymbol{\theta}_t) \right) + \Gamma(\boldsymbol{\theta}_t) \right] + \boldsymbol{\eta}_t G(\boldsymbol{\theta}_t) \quad (13)$$

where $\Gamma_i = \sum_j \frac{\partial G_{i,j}(\boldsymbol{\theta})}{\partial \theta_j}$ describes how the preconditioner changes with respect to $\boldsymbol{\theta}$.

We can then obtain the posterior approximately with a set of $\Theta = [\boldsymbol{\theta}_1, \boldsymbol{\theta}_2, \dots, \boldsymbol{\theta}_n]$ after n updates from pSGLD. Then, the approximation of Eq. (11) can be obtained by a Bayesian model average [65].

A.2 Gaussian process regression

A.2.1 Gaussian process regression with explicit basis function

GPR is a kernel machine learning method that can be viewed as the generalized form of Bayesian linear regression or a BNN with one infinite hidden layer, where the prior distribution is a standard Normal distribution [14]. A general format of a GPR can be expressed as follows when using the function space view and assuming a mean function given by a linear model (on the weights $\boldsymbol{\beta}$):

$$f(\mathbf{x}) = \mathbf{h}(\mathbf{x})^T \boldsymbol{\beta} + \delta(\mathbf{x}) \quad (14)$$

where $\mathbf{h}(\mathbf{x})$ is a set of basis function, i.e. $\mathbf{h}(\mathbf{x}) = [1, \mathbf{x}, \mathbf{x}^2, \dots]^T$ where the length is set to be M ; $\delta(\mathbf{x})$ is a GPR with zero mean expressed as $\mathcal{GP}(0, k(\mathbf{x}, \mathbf{x}))$, $\boldsymbol{\beta}$ is a set of additional parameters that used to tune basis function for minimizing the residual between $\mathbf{h}(\mathbf{x})^T \boldsymbol{\beta}$ and \mathbf{y} (see Fig. 1). The parameters within the covariance function and $\boldsymbol{\beta}$ are determined by maximum likelihood estimation referred to Appendix. A.2.2. The predictions³ of the general GPR considering the effect brought by the explicit basis function can then be expressed as^{4,5}:

$$f(\mathbf{x}') = \mathbf{h}(\mathbf{x}')^T \hat{\boldsymbol{\beta}} + \mathbf{k}(\mathbf{x}', \mathbf{X}) \mathbf{K}(\mathbf{X}, \mathbf{X})^{-1} (\mathbf{y} - \mathbf{h}(\mathbf{X})^T \hat{\boldsymbol{\beta}}) \quad (15)$$

$$s_f^2(\mathbf{x}') = k(\mathbf{x}', \mathbf{x}') - \mathbf{k}(\mathbf{x}', \mathbf{X}) \mathbf{K}(\mathbf{X}, \mathbf{X})^{-1} \mathbf{k}(\mathbf{X}, \mathbf{x}') + \mathbf{r}^T (\mathbf{h}(\mathbf{X}) \mathbf{K}(\mathbf{X}, \mathbf{X})^{-1} \mathbf{h}(\mathbf{X})^T)^{-1} \mathbf{r} \quad (16)$$

where $\mathbf{r} = \mathbf{h}(\mathbf{x}') - \mathbf{h}(\mathbf{X}) \mathbf{K}(\mathbf{X}, \mathbf{X})^{-1} \mathbf{k}(\mathbf{X}, \mathbf{x}')$. The first two terms are predictive variance deduced by the zero mean GPR and the third term is the predictive variance caused by the explicit basis function.

Incorporating explicit basis functions helps the GPR to generalize for more complicated problems, while one has to select the basis function $\mathbf{h}(\mathbf{x})$ beforehand or use symbolic regression to identify the terms [66].

A.2.2 Parameters estimation

Assuming the outputs \mathbf{y} follow a Normal distribution, if a GPR with explicit basis functions is employed, the marginal likelihood can be formulated as [14]:

$$L(\mathbf{y}|\boldsymbol{\beta}, \boldsymbol{\theta}) = \frac{1}{\sqrt{(2\pi)^n |\mathbf{K}|}} \exp \left(-\frac{1}{2} (\mathbf{y} - \mathbf{h}(\mathbf{X})^T \boldsymbol{\beta})^T \mathbf{K}^{-1} (\mathbf{y} - \mathbf{h}(\mathbf{X})^T \boldsymbol{\beta}) \right) \quad (17)$$

Then, the log marginal likelihood can be expressed by:

$$\ln L(\mathbf{y}|\boldsymbol{\beta}, \boldsymbol{\theta}) = -\frac{n}{2} \ln(2\pi) - \frac{1}{2} \ln |\mathbf{K}| - \frac{(\mathbf{y} - \mathbf{h}(\mathbf{X})^T \boldsymbol{\beta})^T \mathbf{K}^{-1} (\mathbf{y} - \mathbf{h}(\mathbf{X})^T \boldsymbol{\beta})}{2} \quad (18)$$

³For simplification, Eqs. (15) and (16) are derived assuming that $\boldsymbol{\beta}$ is a deterministic value rather than another distribution. Readers can find more information in [14] for cases where $\boldsymbol{\beta}$ also follows a distribution.

⁴Eqs. (15) and (16) assume no noise in observations. If the response has noise that is independent identically distributed and Gaussian ε with variance σ^2 , the kernel function should have one extra term to characterize noise. To this end, the noise kernel function can be written as $\mathbf{K}_{noisy}(\mathbf{X}, \mathbf{X}) = \mathbf{K}(\mathbf{X}, \mathbf{X}) + \sigma^2 \mathbf{I}$

⁵Naming convention: $k(\mathbf{x}, \mathbf{x})$ represents a number; $\mathbf{k}(\mathbf{x}, \mathbf{X})$ represents a $1 \times n$ vector and vice versa; $\mathbf{K}(\mathbf{X}, \mathbf{X})$ is a $n \times n$ matrix. Moreover, the default vector is a column vector.

By taking derivatives of Eq. (18) and setting to zero, we obtain maximum likelihood estimation for β .

$$\hat{\beta} = \left(\mathbf{h}(\mathbf{X})\mathbf{K}^{-1}\mathbf{h}(\mathbf{X})^T \right)^{-1} \mathbf{h}(\mathbf{X})\mathbf{K}^{-1}\mathbf{y} \quad (19)$$

Now the maximum likelihood estimations $\hat{\beta}$ can be substituted back into Eq. (18) and constant terms removed to give the concentrated ln-likelihood function:

$$\ln L(\mathbf{y}|\boldsymbol{\theta}) = -\frac{1}{2} \ln |\mathbf{K}| - \frac{(\mathbf{y} - \mathbf{h}(\mathbf{X})^T \hat{\beta})^T \mathbf{K}^{-1} (\mathbf{y} - \mathbf{h}(\mathbf{X})^T \hat{\beta})}{2} \quad (20)$$

The value of Eq. (20) is determined by parameter $\boldsymbol{\theta}$, the maximum value can not be found analytically. Therefore, heuristic algorithms can be utilized to find the optimum value of $\boldsymbol{\theta}$.

B KRR-LR-GPR parameter estimation and prediction

The parameter estimation of KRR-LR-GPR involves two stages, the first stage is to determine parameters for LF kernel regression, and the second is to tune parameters for the transfer-learning model and residual GPR.

B.1 LF-KRR parameter estimation

Kernel ridge regression based on the LF dataset can be defined by

$$\mathbf{y}^l = \mathbf{K}(\mathbf{X}^l, \mathbf{X}^l) \mathbf{w} \quad (21)$$

where \mathbf{w} are the weights determined by LF data points, $\mathbf{K}(\mathbf{X}^l, \mathbf{X}^l)$ is a $N^l \times N^l$ Gram or covariance matrix with $\mathbf{K}_{ij} = k(\mathbf{x}_i^l, \mathbf{x}_j^l)$. The value of \mathbf{w} can be determined analytically:

$$\mathbf{w} = \mathbf{K}(\mathbf{X}^l, \mathbf{X}^l)^{-1} \mathbf{y}^l \quad (22)$$

If the data has noise, $\mathbf{w} = (\mathbf{K}(\mathbf{X}^l, \mathbf{X}^l) + \lambda \mathbf{I})^{-1} \mathbf{y}^l$ where λ is the LF noise precision.

B.2 Transfer-learning model and residual GPR parameter estimation

Regarding the parameter estimation of the transfer-learning model and residual GPR, it follows the same procedure as Section A.2.2, where the log marginal likelihood function can be formulated as:

$$\ln L(\mathbf{y}^h | \boldsymbol{\rho}, \boldsymbol{\theta}^h) = -\frac{N^h}{2} \ln(2\pi) - \frac{1}{2} \ln |\mathbf{K}(\mathbf{X}^h, \mathbf{X}^h)| - \frac{(\mathbf{y}^h - \mathbf{m}(\mathbf{X}^h)^T \boldsymbol{\rho})^T \mathbf{K}(\mathbf{X}^h, \mathbf{X}^h)^{-1} (\mathbf{y}^h - \mathbf{m}(\mathbf{X}^h)^T \boldsymbol{\rho})}{2} \quad (23)$$

By taking the derivative of Eq. (23) and setting it to zero, we can get the estimation of $\hat{\boldsymbol{\rho}}$:

$$\hat{\boldsymbol{\rho}} = (\mathbf{m}(\mathbf{X}^h) \mathbf{K}(\mathbf{X}^h, \mathbf{X}^h)^{-1} \mathbf{m}(\mathbf{X}^h)^T)^{-1} \mathbf{m}(\mathbf{X}^h) \mathbf{K}(\mathbf{X}^h, \mathbf{X}^h)^{-1} \mathbf{y}^h \quad (24)$$

Then, optimizing the ln-concentrated function for optimal $\boldsymbol{\theta}^h$

$$\ln L(\mathbf{y}^h | \boldsymbol{\theta}^h) = -\frac{1}{2} \ln |\mathbf{K}(\mathbf{X}^h, \mathbf{X}^h)| - \frac{(\mathbf{y}^h - \mathbf{m}(\mathbf{X}^h)^T \hat{\boldsymbol{\rho}})^T \mathbf{K}(\mathbf{X}^h, \mathbf{X}^h)^{-1} (\mathbf{y}^h - \mathbf{m}(\mathbf{X}^h)^T \hat{\boldsymbol{\rho}})}{2} \quad (25)$$

B.3 Predictions

We can obtain the predictions of KRR-LR-GPR by modifying Eqs. 14 and 16 into:

$$f^h(\mathbf{x}') = \mathbf{m}(\mathbf{x}')^T \hat{\boldsymbol{\rho}} + \mathbf{k}(\mathbf{x}', \mathbf{X}^h) \mathbf{K}(\mathbf{X}^h, \mathbf{X}^h)^{-1} (\mathbf{y}^h - \mathbf{m}(\mathbf{X}^h)^T \hat{\boldsymbol{\rho}}) \quad (26)$$

$$s_{f^h}^2(\mathbf{x}') = k(\mathbf{x}', \mathbf{x}') - \mathbf{k}(\mathbf{x}', \mathbf{X}^h) \mathbf{K}(\mathbf{X}^h, \mathbf{X}^h)^{-1} \mathbf{k}(\mathbf{X}^h, \mathbf{x}') + \mathbf{r}^T (\mathbf{m}(\mathbf{X}^h) \mathbf{K}(\mathbf{X}^h, \mathbf{X}^h)^{-1} \mathbf{m}(\mathbf{X}^h)^T)^{-1} \mathbf{r} \quad (27)$$

where $\mathbf{r} = \mathbf{m}(\mathbf{x}') - \mathbf{m}(\mathbf{X}^h) \mathbf{K}(\mathbf{X}^h, \mathbf{X}^h)^{-1} \mathbf{k}(\mathbf{X}^h, \mathbf{x}')$.

C Numerical functions

C.1 Numerical functions for testing KRR-LR-GPR

This section includes details on the low-dimensional numerical functions considered in this paper. Originally, those functions were single fidelity functions used to verify optimization algorithms [67]. They were extended by Jiang et al [68], Sander et al. [69] and Mainini et al. [70] for verifying the performance of MF optimization algorithms.

- Forrester function

$$f^h(x) = (6x - 2)^2 \sin(12x - 4) \quad (28)$$

$$f^l(x) = A(6x - 2)^2 \sin(12x - 4) + B(x - 0.5) - C \quad (29)$$

where $x \in [0, 1]$. By selecting different values of A , B , and C , LF functions with different correlations to the HF function. Three different configurations are adopted in Section 4.1 where $lf1$ considers $A = 1, B = 0, C = 5$; $lf2$ considers $A = 0.5, B = 10, C = 5$; $lf3$ considers $A = 0.1, B = 10, C = 0.1$.

- Hartman3 function

$$f^h(\mathbf{x}) = - \sum_{i=1}^4 c_i \exp \left(- \sum_{j=1}^3 a_{ij} (x_j - p_{ij})^2 \right) \quad (30)$$

$$f^l(\mathbf{x}) = 0.585 - 0.324x_1 - 0.379x_2 - 0.431x_3 \quad (31)$$

$$- 0.208x_1x_2 + 0.326x_1x_3 + 0.193x_2x_3 + 0.225x_1^2 + 0.263x_2^2 + 0.274x_3^2 \quad (32)$$

where

$$\mathbf{c} = \begin{bmatrix} 1 \\ 1.2 \\ 3 \\ 3.2 \end{bmatrix}, \quad \mathbf{p} = \begin{bmatrix} 0.3689 & 0.117 & 0.2673 \\ 0.4699 & 0.4387 & 0.747 \\ 0.1091 & 0.8732 & 0.5547 \\ 0.03815 & 0.5743 & 0.8828 \end{bmatrix}, \quad \mathbf{a} = \begin{bmatrix} 3 & 10 & 30 \\ 0.1 & 10 & 35 \\ 3 & 10 & 30 \\ 0.1 & 10 & 35 \end{bmatrix}$$

where $\mathbf{x} \in [0, 1]$

- Hartman6 function

$$f^h(\mathbf{x}) = - \sum_{i=1}^4 c_i \exp \left(- \sum_{j=1}^6 a_{ij} (x_j - p_{ij})^2 \right) \quad (33)$$

$$f^l(\mathbf{x}) = - \sum_{i=1}^4 c_i \exp \left(- \sum_{j=1}^6 a_{ij} (l_j x_j - p_{ij})^2 \right) \quad (34)$$

where

$$\mathbf{p} = \begin{bmatrix} 0.1312 & 0.1696 & 0.5569 & 0.0124 & 0.8283 & 0.5886 \\ 0.2329 & 0.4135 & 0.8307 & 0.3736 & 0.1004 & 0.9991 \\ 0.2348 & 0.1451 & 0.3522 & 0.2883 & 0.3047 & 0.6650 \\ 0.4047 & 0.8828 & 0.8732 & 0.5743 & 0.1091 & 0.0381 \end{bmatrix}, \quad \mathbf{c} = \begin{bmatrix} 1.0 \\ 1.2 \\ 3.0 \\ 3.2 \end{bmatrix},$$

$$\mathbf{a} = \begin{bmatrix} 10.00 & 3.0 & 17.00 & 3.5 & 1.7 & 8 \\ 0.05 & 10.0 & 17.00 & 0.1 & 8.0 & 14 \\ 3.00 & 3.5 & 1.70 & 10.0 & 17.0 & 8 \\ 17.00 & 8.0 & 0.05 & 10.0 & 0.1 & 14 \end{bmatrix}, \quad \mathbf{l} = \begin{bmatrix} 0.75 \\ 1.0 \\ 0.8 \\ 1.3 \\ 0.7 \\ 1.1 \end{bmatrix}$$

where $\mathbf{x} \in [0, 1]$

- Six-hump function

$$f^h(\mathbf{x}) = (4 - 2.1x_1^2 + \frac{x_1^4}{3})x_1^2 + x_1x_2 - 4x_2^2 \quad (35)$$

$$f^l(\mathbf{x}) = f^h(0.7\mathbf{x}) - x_1x_2 - 15 \quad (36)$$

where $\mathbf{x} \in [-2, 2]$

- Bohachevsky function

$$f^h(\mathbf{x}) = (x_1^2 + 2x_2^2 - 0.3 \cos(3\pi x_1) - 0.4 \cos(4\pi x_2) + 0.7)^2 \quad (37)$$

$$f^l(\mathbf{x}) = f^h(0.7x_1, x_2) + x_1x_2 - 12 \quad (38)$$

where $\mathbf{x} \in [-5, 5]$

- Booth function

$$f^h(\mathbf{x}) = (x_1^2 + 2x_2^2 - 7)^2 + (2x_1^2 + x_2 - 5)^2 \quad (39)$$

$$f^l(\mathbf{x}) = f_h(0.4x_1, x_2) + 1.7 \cdot x_1x_2 - x_1 + 2x_2 \quad (40)$$

where $\mathbf{x} \in [-10, 10]$

- Borehole function

$$f^b(\mathbf{x}, A, B) = \frac{AT_u(H_u - H_l)}{\log\left(\frac{r}{r_w}\right) \left(1 + \frac{2LT_u}{\log\left(\frac{r}{r_w}\right)r_w^2K_w} + \frac{T_u}{T_l}\right)} \quad (41)$$

$$f^h(\mathbf{x}) = f^b(\mathbf{x}, 2\pi, 1) \quad (42)$$

$$f^l(\mathbf{x}) = f^b(\mathbf{x}, 5, 1.5) \quad (43)$$

where

$$rw \in [0.05, 0.15]$$

$$r \in [100, 50000]$$

$$Tu \in [63070, 115600]$$

$$Hu \in [990, 1110]$$

$$Tl \in [63.1, 116]$$

$$Hl \in [700, 820]$$

$$L \in [1120, 1680]$$

$$Kw \in [9855, 12045]$$

- CurrinExp function

$$f^h(x_1, x_2) = (1 - \exp(-1/(2x_2))) \times \frac{2300x_1^3 + 1900x_1^2 + 2092x_1 + 60}{100x_1^3 + 500x_1^2 + 4x_1 + 20} \quad (44)$$

$$f^l(x_1, x_2) = \frac{1}{4} [f^h(x_1 + 0.05, x_2 + 0.05) + f^h(x_1 + 0.05, x_2 - 0.05)] \\ + \frac{1}{4} [f^h(x_1 - 0.05, x_2 + 0.05) + f^h(x_1 - 0.05, x_2 - 0.05)] \quad (45)$$

where $\mathbf{x} \in [0, 1]$

- Park91A function

$$f^h(\mathbf{x}) = \frac{x_1}{2} \left(\sqrt{1 + (x_2 + x_3^2) \frac{x_4}{x_1^2} - 1} \right) + (x_1 + 3x_4)e^{1+\sin(x_3)} \quad (46)$$

$$f^l(\mathbf{x}) = (1 + \sin(x_1)/10)f^h(\mathbf{x}) - 2x_1 + x_2^2 + x_3^2 + 0.5 \quad (47)$$

where $\mathbf{x} \in [0, 1]$

- Park91B function

$$f^h(\mathbf{x}) = \frac{2}{3}e^{x_1+x_2} - x_4 \sin(x_3) + x_3 \quad (48)$$

$$f^l(\mathbf{x}) = 1.2f^h(\mathbf{x}) - 1 \quad (49)$$

where $\mathbf{x} \in [0, 1]$

C.2 Numerical functions for testing DNN-LR-BNN

- 1D illustrative function [13]

$$f^h(\mathbf{x}) = (x - \sqrt{2}) \sin(8\pi x)^2 \quad (50)$$

$$f^{l1}(\mathbf{x}) = \sin(8\pi x) \quad (51)$$

$$f^{l2}(\mathbf{x}) = 1.2f^h(\mathbf{x}) - 0.5 \quad (52)$$

$$f^{l3}(\mathbf{x}) = \sin(16\pi x)^2 \quad (53)$$

$$(54)$$

where $x \in [0, 1]$. In the illustrative case, both LF and HF data are assumed to be corrupted by white noise with $\mathcal{N}(0, 0.05^2)$.

- 4D function [13]

$$f^h(\mathbf{x}) = \frac{1}{2}(0.1 \exp(x_1 + x_2) - x_4 \sin(12\pi x_3) + x_3) \quad (55)$$

$$f^l(\mathbf{x}) = 1.2f^h(\mathbf{x}) - 0.5 \quad (56)$$

where $x \in [0, 1]$. The LF has noise with $\mathcal{N}(0, 0.05^2)$ and HF has noise with $\mathcal{N}(0, 0.01^2)$

- high dimensional function

The high dimensional function used in [43] is adopted, which can be expressed by

$$f^h(\mathbf{x}) = \sum_{i=2}^{20} (2x_i^2 - x_{i-1})^2 + (x_1 - 1)^2 \quad (57)$$

$$f^l(\mathbf{x}) = 0.8f^h(\mathbf{x}) + \sum_{i=2}^{20} 0.4x_{i-1}x_i - 50 \quad (58)$$

where $x \in [-3, 3]$. We set the dimension in [20, 50, 100] to challenge DNN-LR-BNN in high-dimensional problems. Moreover, this function is assumed to have zero noise in LF and HF has noise with $\mathcal{N}(0, 50^2)$.

D Additional experiments for KRR-LR-GPR

D.1 Additional results of KRR-LR-GPR comprehensive experiments

In section 4.1.2, we only show the results of the Booth function, and the remaining comparison results are shown in Fig.12 and Fig. 13.

D.2 Experiments with noiseless data-scarce HF and low-dimensional problems: KRR-LR-GPR

As reported in the literature [31] and to the best of our knowledge, the existing multi-fidelity GPR methods have been considered for noiseless problems, which is a special case in this paper where $\sigma^h = 0$ and $\sigma^l = 0$. To demonstrate the effectiveness of the KRR-LR-GPR in those cases, we present an illustrative example based on the typical multi-fidelity case presented by Forrester [23], the predictive performance of KRR-LR-GPR compared to other multi-fidelity GPR approaches is presented in Fig. 14 and different performance metrics for this problem are included in Table 7.

Table 7: Results comparison of the noiseless illustrative example

Methods	NRMSE	R2 Score	LF training time (s)	HF training time (s)
Hierarchical Kriging	0.0221	0.9998	0.06014	0.0535
Co-Kriging	0.0220	0.9998	0.4148	0.4708
Scaled Kriging	0.9723	0.6812	0.3952	0.0942
KRR-LR-GPR	0.0054	1.0000	0.0007	0.0515

We can observe that the findings are the same as the results reported in Fig 3 and Table 2. KRR-LR-GPR has a slightly better performance compared with other multi-fidelit GPR approaches. Other than that, for this simple example, one can already see that KRR-LR-GPR is faster to train, only requiring 0.0007 s for the LF model.

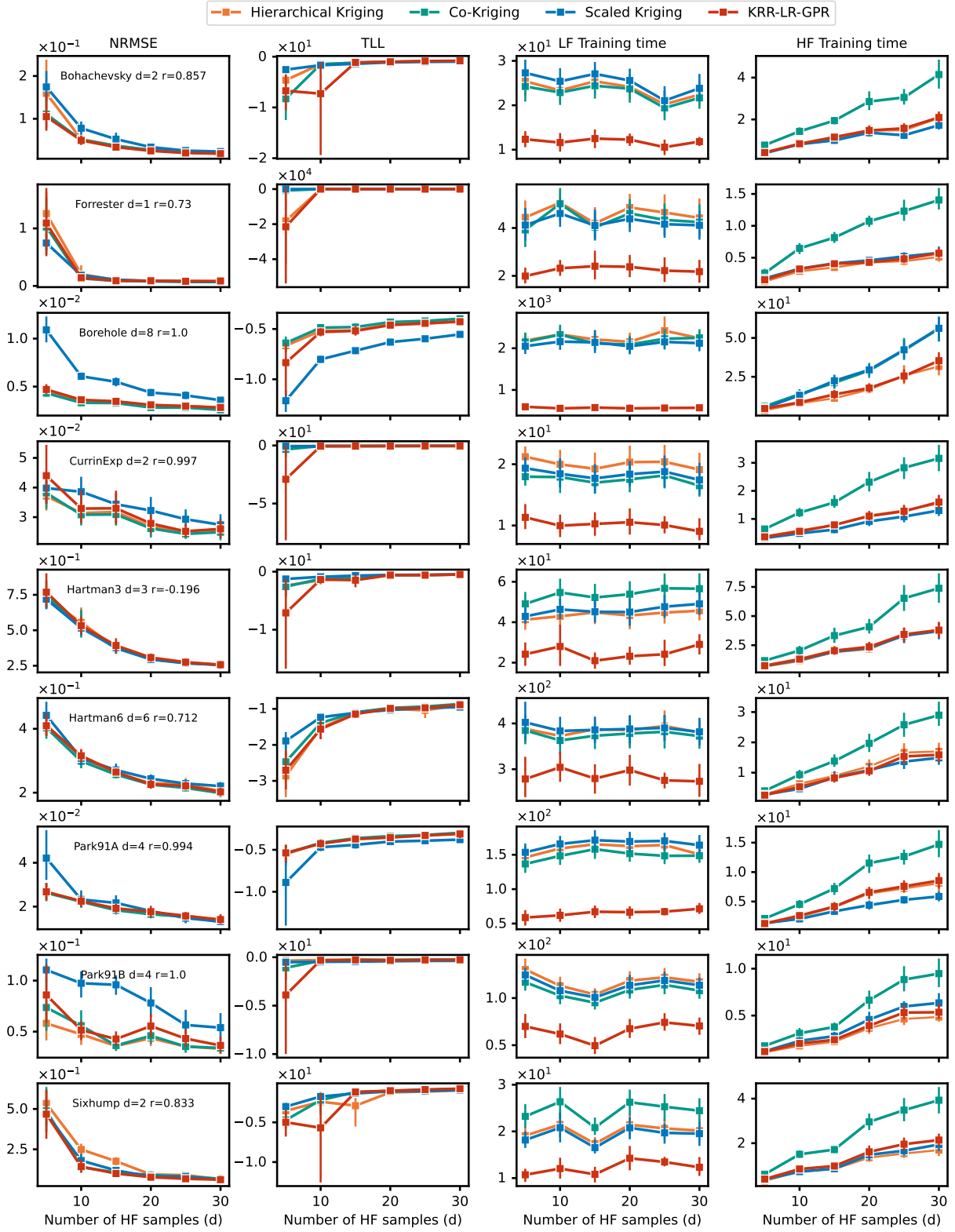


Figure 12: Additional comprehensive experiment results of KRR-LR-GPR with different amounts of HF data. Different colors represent different methods, where NRMSE is the smaller the better and TLL is the larger the better.

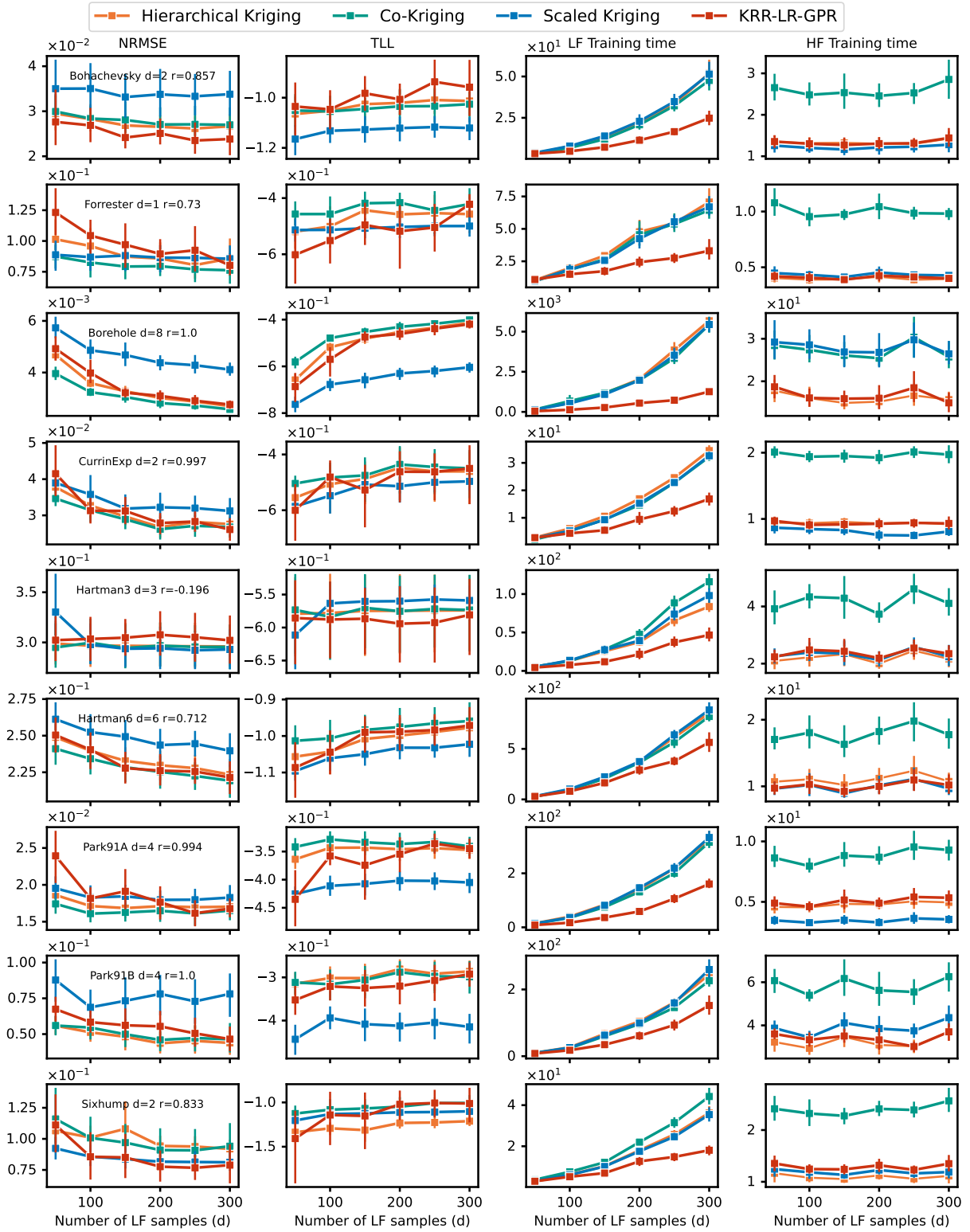


Figure 13: Additional comprehensive experiment results of KRR-LR-GPR with different amounts of LF data. Different colors represent different methods, where NRMSE is the smaller the better and TLL is the larger the better.

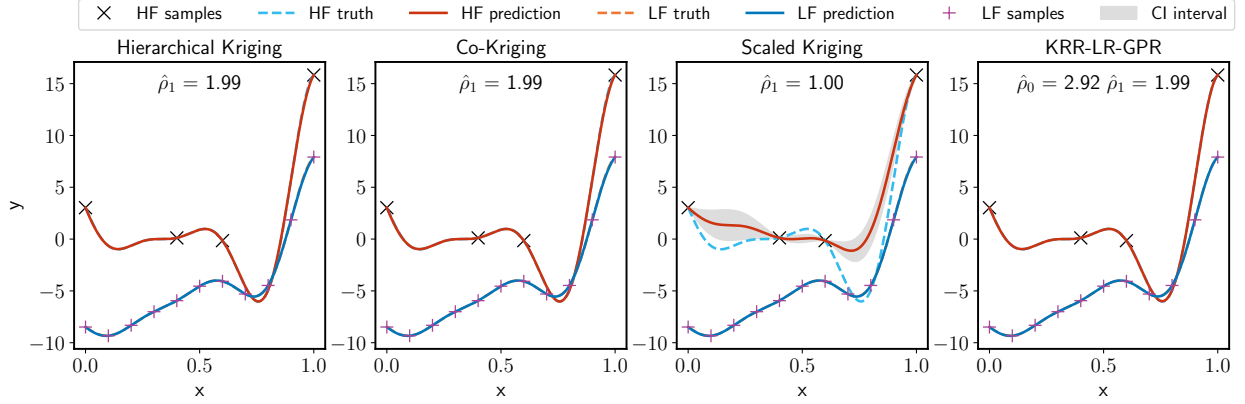


Figure 14: Fitting performance of MF models on noiseless illustrative example

E Ablation studies of KRR-LR-GPR

E.1 Influence of LF polynomial order to KRR-LR-GPR

We provide an opportunity to select different polynomial orders of the LF surrogate in Eq. (4) and Fig. 1. We conducted an ablation study on how the selection of $\mathbf{m}(\mathbf{x})$ would influence the performance of the KRR-LR-GPR⁶. Fig.15 shows the fitting performance on an illustrative example, and Table 8 summarizes the corresponding accuracy metric values.

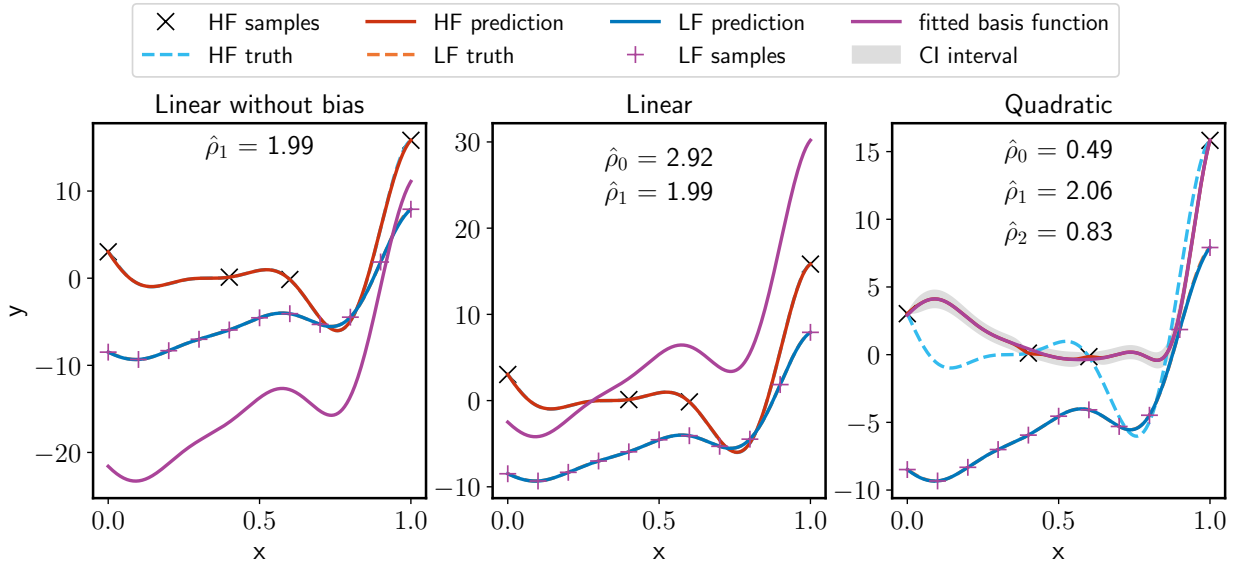


Figure 15: Performance of KRR-LR-GPR based on different LF polynomial orders

Table 8: Results comparison of KRR-LR-GPR based on different LF polynomial orders

LF polynomial order	NRMSE	R2 Score	LF training time	HF training time
Linear without bias	0.0237	0.9998	0.0063	0.0730
Linear	0.0072	1.0000	0.0004	0.0512
Quadratic	1.1362	0.5646	0.0004	0.1641

With quadratic LF features, the KRR-LR-GPR overfits the Forrester function, though $\mathbf{m}(\mathbf{x})\rho$ have a small residual to y^h . On the other hand, KRR-LR-GPR can fit the Forrester function well with the linear LF feature, where we observe

⁶To eliminate the influence of noise, the experiment is conducted with datasets without noise.

that the bias does influence the value of ρ_1 , but shifts the entire LF surrogate closer to the HF data. As listed in Table 8 the bias term ρ_0 also improves accuracy. To gain a deeper understanding of the effect of the LF polynomial order, Fig. 16 gives the NRMSE changes as the HF sample increases on the set of test examples.

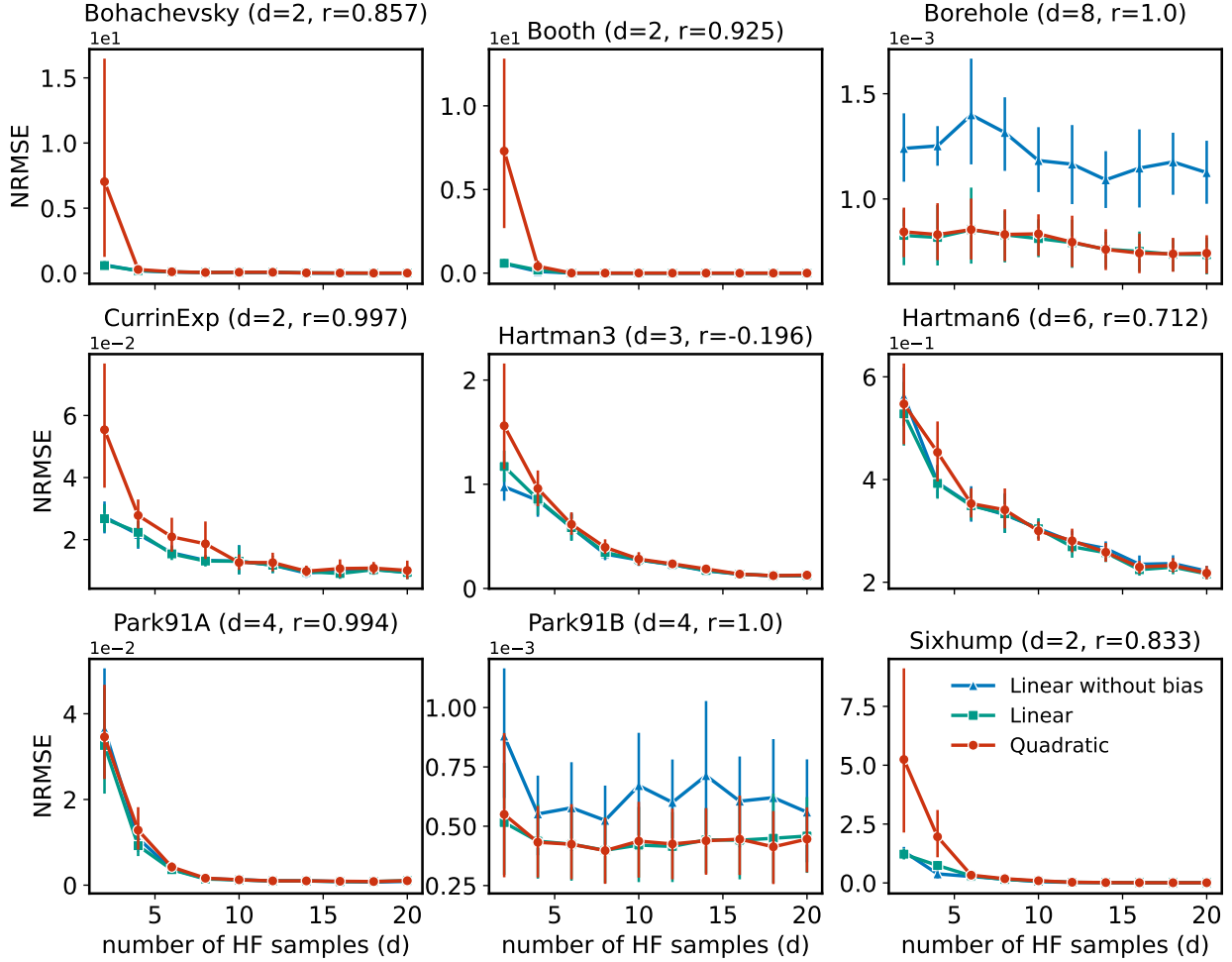


Figure 16: NRMSE of MF-RBF-Kriging based on different LF polynomial orders (LF data $100 \times d$)

As shown in Fig. 16, KRR-LR-GPR with quadratic LF polynomial order has large errors, leading to overfitting in most cases when the number of LF samples is smaller. The cases with linear polynomial order alleviate this issue to some extent. Regarding the effect of the bias term ρ_0 , it does not influence most of the cases, whereas it brings improvements in some cases like *Borehole* and *Park91A*. Moreover, the bias term has slight positive effects on KRR-LR-GPR when LF samples are less in most cases. To this end, we adopt $\mathbf{m}(\mathbf{x}) = [1, f^l(\mathbf{x})]^T$ in this paper.

E.2 Influence of HF-to-LF correlation and HF noise level on KRR-LR-GPR

KRR-LR-GPR converges to good accuracy with more HF data as shown in Section 4.1.2, while differences exist among different examples due to the HF-to-LF correlation, see Appendix D.1. We fix the noise level to be $\sigma^h = 0.3$ in Section 4.1.2. Therefore, we design the ablation study here to investigate the influence of the HF-to-LF correlation and the HF noise level on KRR-LR-GPR compared to GPR. Fig.17 depicts the corresponding results.

We can see from Fig. 17 that the HF noise level has a significant impact on KRR-LR-GPR, where larger HF noise levels would deteriorate the performance even with an adequate amount of HF data. In addition, higher HF-to-LF correlations are preferred when utilizing KRR-LR-GPR, where clear advantages are observed on both NRMSE and TLL. Conversely, poor HF-to-LF correlation decreases the performance of KRR-LR-GPR.

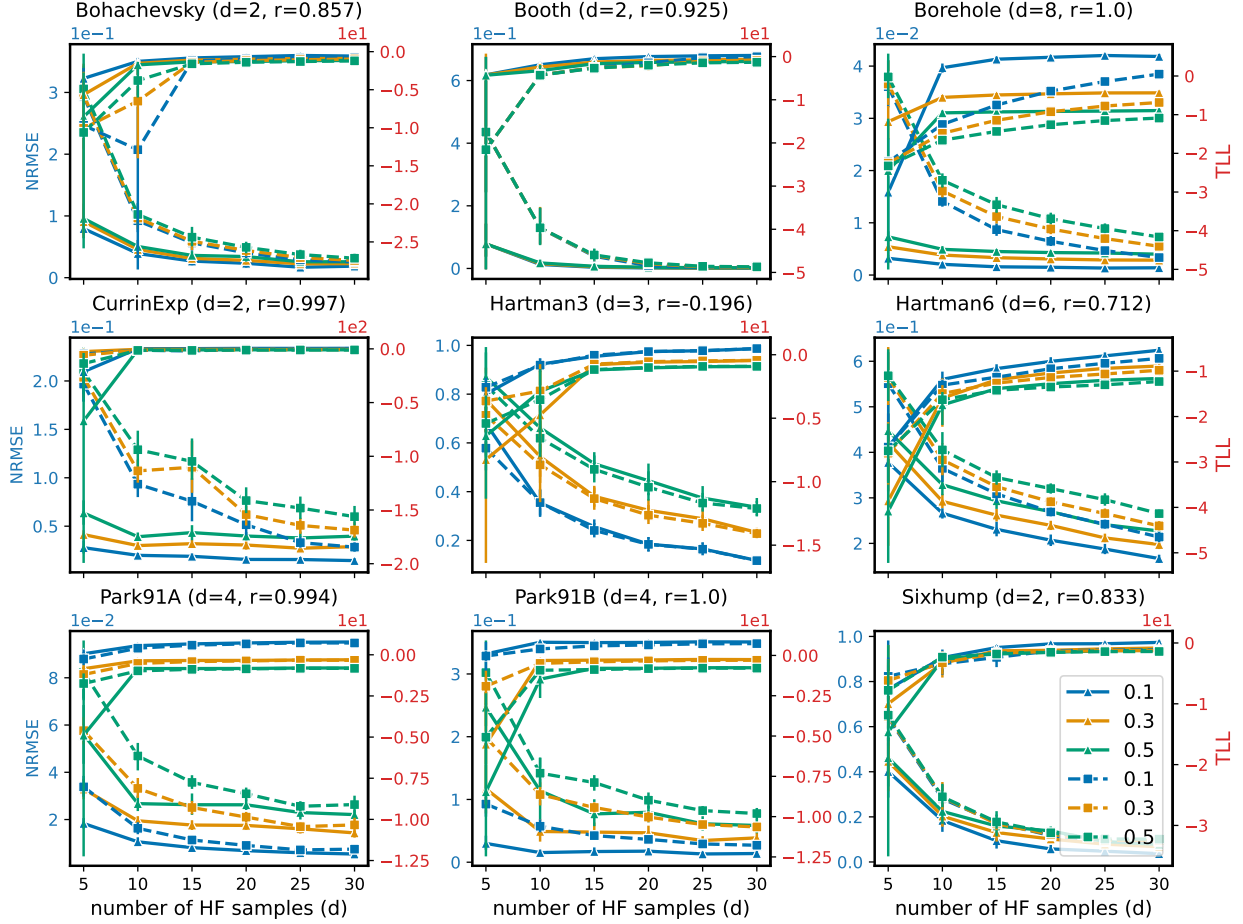


Figure 17: NRMSE and TLL of different examples with increasing HF data (LF data $200 \times d$): The solid and dash lines represent KRR-LR-GPR and GPR respectively, and line color shows different HF noise levels

E.3 Influence of HF and LF samples on KRR-LR-GPR

Section 4.1.2 included two experiments using a fixed number of HF or LF samples and explored the effect of another factor. To have a better overview of how HF and LF samples influence the KRR-LR-GPR method, Fig.18⁷ shows the whole design of experiments instead of slices shown in Figs.7 and 8.

In Fig.18, R2 Score is primarily influenced by the number of HF samples and the LF samples will improve the robustness of KRR-LR-GPR. The training time plotted at the right heatmap is the total training time for both HF and LF models, more CPU time is needed with a greater total amount of data. However, the influence of HF data on execution time is more critical than that of LF data.

F Hyperparameters of experiments on DNN-LR-BNN

F.1 Hyperparameters of the experiments

Hyperparameters and sampling points used for training the DNN-LR-BNN and DNN-BNN models are described in Table 9. These experiments were extracted from references [43, 13, 44] for examples of 1D, 4D, and 20D. For the cases of 50D and 100D we adopt the same hyperparameters as for the case of 20D and consider $1000 \times d$ and $100 \times d$ samples for LF and HF, respectively.

⁷The reason why R2 score is selected is that R2 Score does not depend on the actual magnitude of the response.

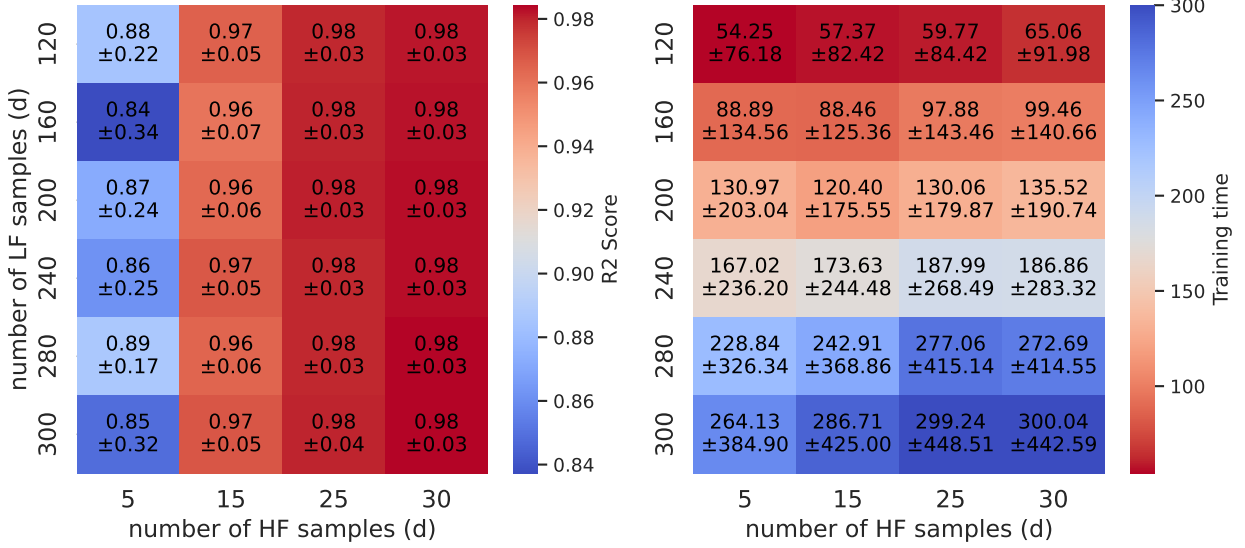


Figure 18: Influence of HF and LF samples on KRR-LR-GPR

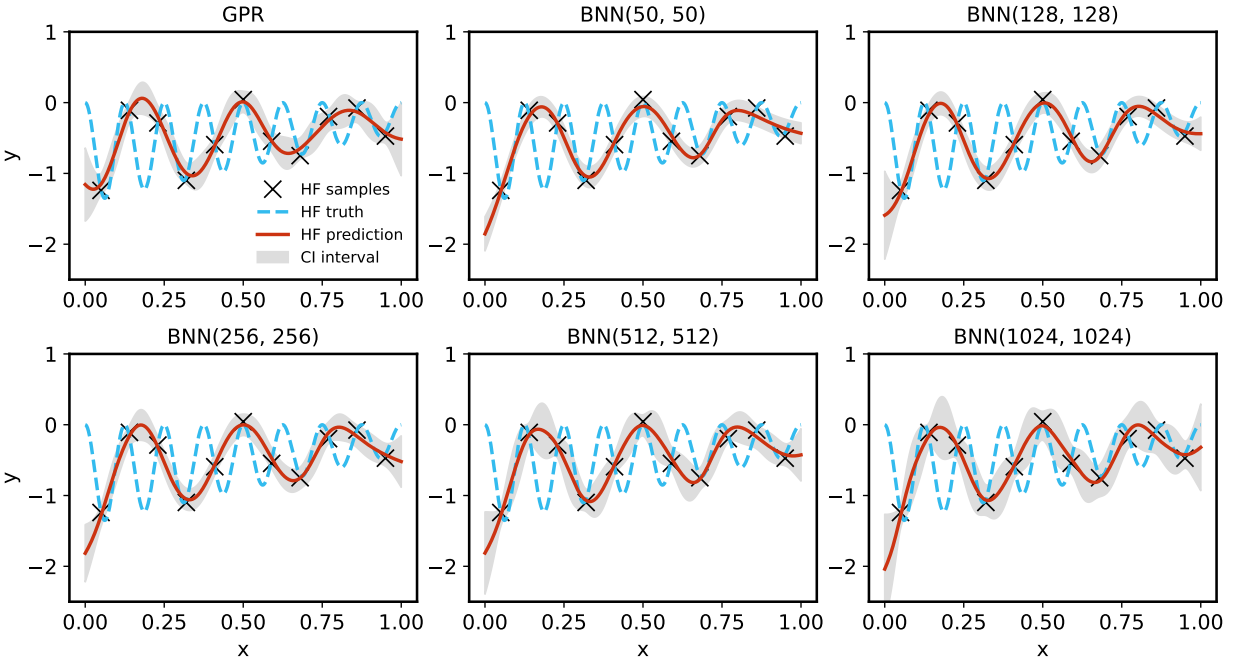


Figure 19: Influence of network architecture on the performance of single-fidelity BNN. All the hyperparameters are fixed as Table 9 except expanding the network from (50, 50) to (1024, 1024) neurons in each of the two hidden layers.

F.2 Influence of neural architecture on the performance of DNN-LR-BNN

We know that hyperparameters are crucial to deep neural networks. Therefore, we conduct a brief study on the influence of neural architecture on the performance of the developed DNN-LR-BNN method based on the illustrative example. First of all, we show that network architecture has a limited impact on the predictive mean but influences the predictive uncertainty significantly as highlighted in Fig. 19. We show the shallow network would be overconfident, meaning a smaller uncertainty bound, while the uncertainty would increase and gradually converge to the case of GPR shown in Fig.19. This is reasonable because GPR is equivalent to an infinitely wide neural network with a single hidden layer [47].

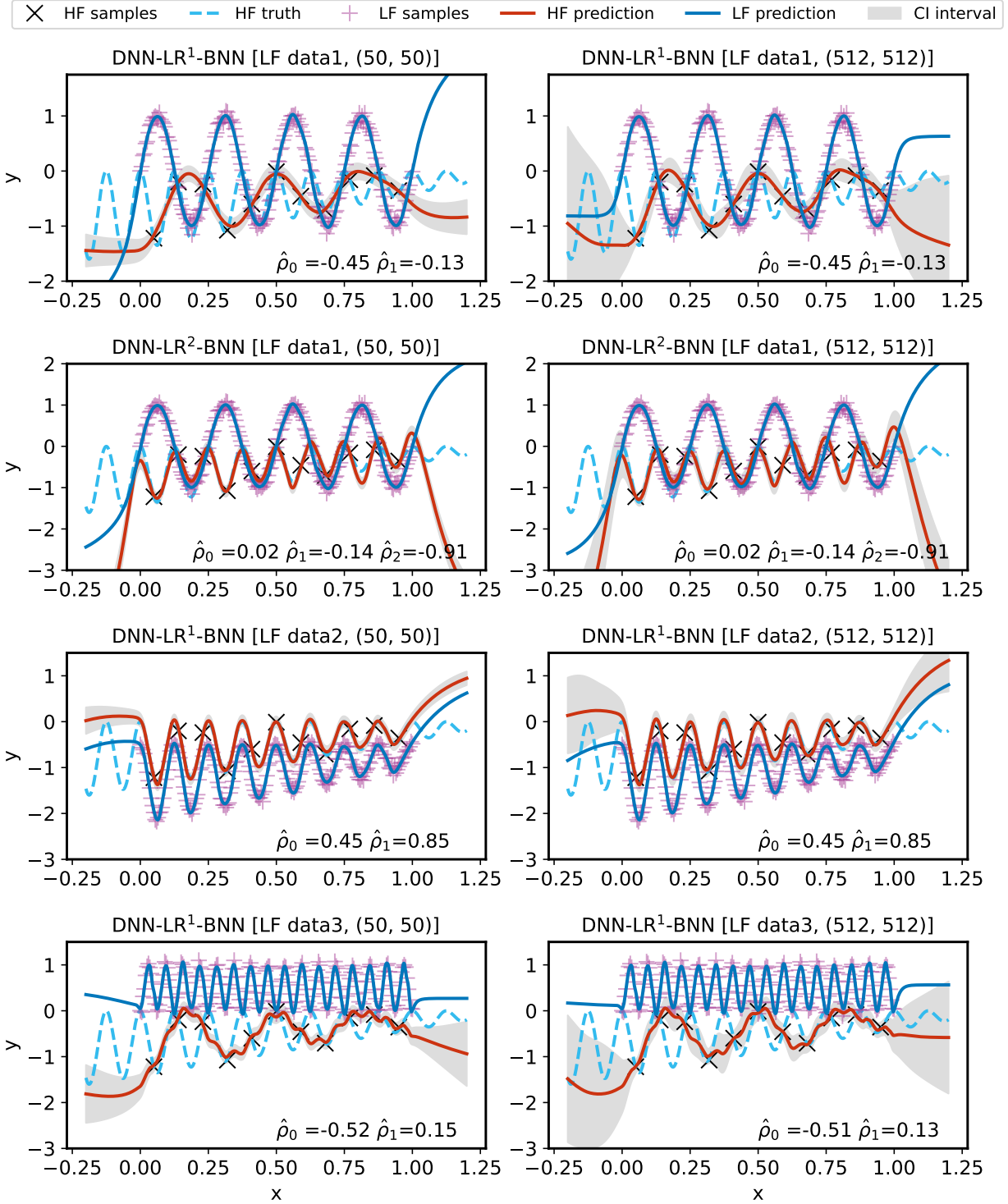


Figure 20: Comparison of DNN-LR-BNN considering two different architectures (left) using 50 neurons, and (right) using 512 neurons in each of the two hidden layers.

Secondly, we compare the corresponding influence of neural architecture on DNN-LR-BNN and DNN-BNN, and their results are depicted in Figs.20 and 21. We observe the same pattern in the results of DNN-LR-BNN when enlarging the neural network architecture. Interestingly, the learned ρ is also robust to the neural network architecture choice.

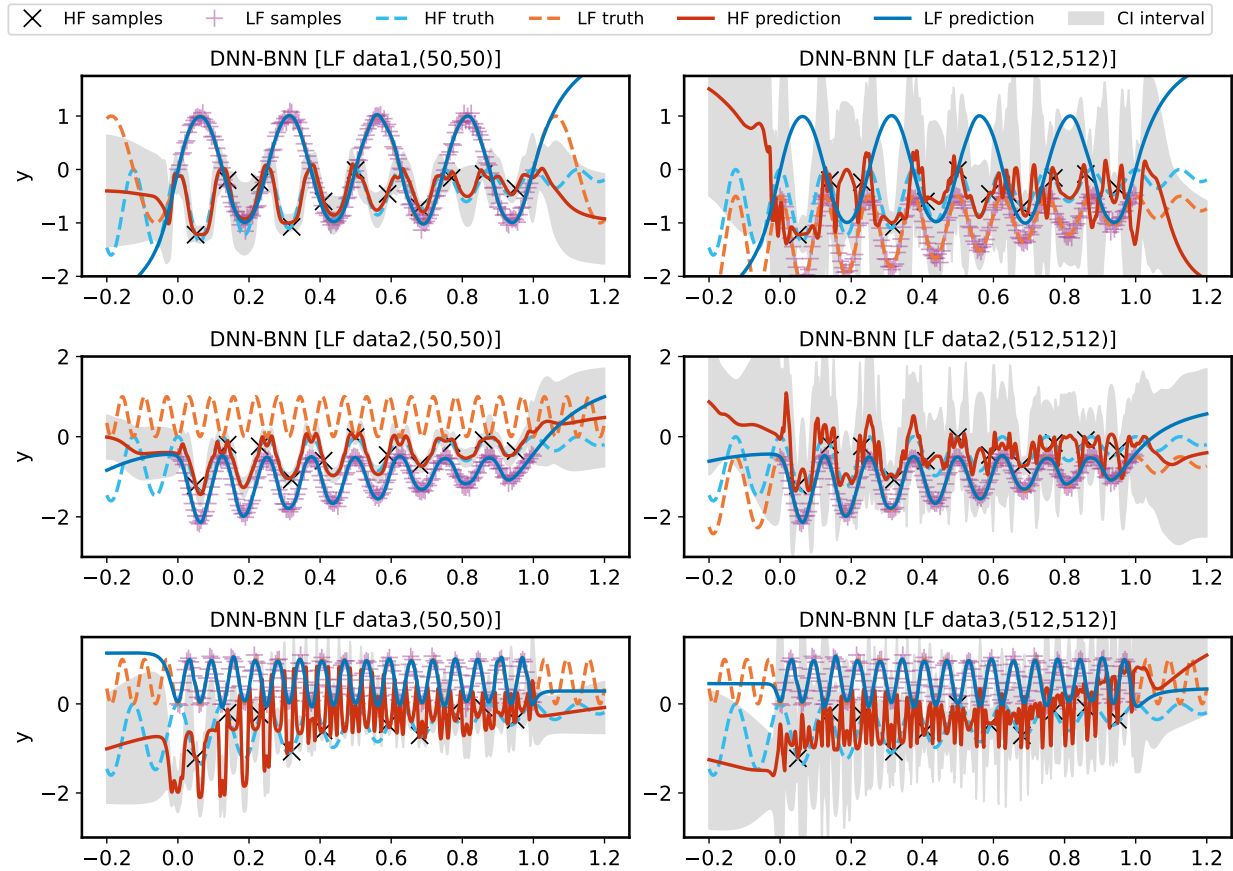


Figure 21: Comparison of DNN-BNN considering two different architectures (left) using 50 neurons, and (right) using 512 neurons in each of the two hidden layers.

However, the DNN-BNN is significantly sensitive to the neural network architecture, leading to reasonable results for small networks but significant overfitting for larger networks.

Table 9: Hyperparameters for the DNN-LR-BNN experiments

Example	Hyperparameter Name	Hyperparameters setting			Samples	
		BNN	DNN-BNN	DNN-LR-BNN		
1D	DNN	Architecture	-	2 hidden, 50 neurons, <i>Tanh</i>	2 hidden, 50 neurons, <i>Tanh</i>	
		Learning Rate	-	10^{-3}	10^{-3}	
		Optimizer	-	Adam	Adam	
		Epoch	-	10000	10000	
	BNN	Architecture	2 hidden, 512 neurons, <i>Tanh</i>	2 hidden, 50 neurons, <i>Tanh</i>	2 hidden, 512 neurons, <i>Tanh</i>	201 LF 11 HF
		Learning rate	0.001	0.001	0.001	
		Posterior collection	300 samples, Burn-in: 20000, Frequency: 100	300 samples, Burn-in: 20000, Frequency: 100	300 samples, Burn-in: 20000, Frequency: 100	
4D	DNN	Architecture	-	2 hidden, 256 neurons, <i>Tanh</i>	2 hidden, 256 neurons, <i>Tanh</i>	
		Learning Rate	-	10^{-3}	10^{-3}	
		Optimizer	-	Adam	Adam	
		Epochs	-	50000	50000	
	BNN	Architecture	2 hidden, 50 neurons, <i>Tanh</i>	2 hidden, 50 neurons, <i>Tanh</i>	2 hidden, 50 neurons, <i>Tanh</i>	25000 LF 150 HF
		Learning Rate	10^{-3}	10^{-3}	10^{-3}	
		Posterior Collection	300 samples, Burn-in: 20000, Frequency: 100	300 samples, Burn-in: 20000, Frequency: 100	300 samples, Burn-in: 20000, Frequency: 100	
20D	DNN	Architecture	-	2 hidden, 200 neurons, <i>Tanh</i>	2 hidden, 200 neurons, <i>Tanh</i>	
		Learning Rate	-	10^{-3}	10^{-3}	
		Optimizer	-	Adam	Adam	
		Epochs	-	80000	80000	
	BNN	Architecture	2 hidden, 512 neurons, <i>ReLU</i>	2 hidden, 512 neurons, <i>ReLU</i>	2 hidden, 512 neurons, <i>ReLU</i>	30000 LF 5000 HF
		Learning Rate	10^{-3}	10^{-3}	10^{-3}	
		Posterior Collection	300 samples, Burn-in: 20000, Frequency: 100	300 samples, Burn-in: 20000, Frequency: 100	300 samples, Burn-in: 20000, Frequency: 100	
50D	DNN	Architecture	-	2 hidden, 256 neurons, <i>Tanh</i>	2 hidden, 256 neurons, <i>Tanh</i>	
		Learning Rate	-	10^{-3}	10^{-3}	
		Optimizer	-	Adam	Adam	
		Epochs	-	50000	50000	
	BNN	Architecture	2 hidden, 512 neurons, <i>ReLU</i>	2 hidden, 512 neurons, <i>ReLU</i>	2 hidden, 512 neurons, <i>ReLU</i>	50000 LF 5000 HF
		Learning Rate	10^{-3}	10^{-3}	10^{-3}	
		Posterior Collection	400 samples, Burn-in: 10000, Frequency: 100	400 samples, Burn-in: 10000, Frequency: 100	400 samples, Burn-in: 10000, Frequency: 100	
100D	DNN	Architecture	-	2 hidden, 256 neurons, <i>Tanh</i>	2 hidden, 256 neurons, <i>Tanh</i>	
		Learning Rate	-	10^{-3}	10^{-3}	
		Optimizer	-	Adam	Adam	
		Epochs	-	50000	50000	
	BNN	Architecture	2 hidden, 512 neurons, <i>ReLU</i>	2 hidden, 512 neurons, <i>ReLU</i>	2 hidden, 512 neurons, <i>ReLU</i>	100000 LF 10000 HF
		Learning Rate	10^{-3}	10^{-3}	10^{-3}	
		Posterior Collection	400 samples, Burn-in: 10000, Frequency: 100	300 samples, Burn-in: 10000, Frequency: 100	400 samples, Burn-in: 10000, Frequency: 100	